Department of Earth and Ocean Sciences
School of Environmental Sciences

MPHIL OF ENVIRONMENTAL SCIENCE
(GEOLOGY AND GEOPHYSICS)

Investigation of lithospheric structure in Mongolia fault: InSAR observations and modelling

Author:
Jing Zhang (200994458)

Supervisor:
Dr. Isabelle Ryder
Prof. Andreas Rietbrock

06/09/2013~20/10/2014

Acknowledgements

Dr. Isabelle Ryder and Prof. Andreas Rietbrock are thanked for being helpful and constructive project supervisors, and particularly, for having patience during instruction for my Matlab improvement. Also thank for Isabelle's lovely music for entertainment during data processing. I thank Lidong Bie, Stephen Hicks, Fuenzalida Velasco Amaya, Garth Tomas, De Angelis Silvio, Larolyn Boucton for geodynamic problem discussion, Yangmao Wen for InSAR methodology discussion. Help from Wang Xiao was important for helping out with computer problem. I am grateful to Fred Pollitz and Yukitoshi Fukahata for using their computer codes. I thank Dr. Hua Wang to help me reprocess the InSAR data using pi-rate software. I would also like to thank Rob Govers for using his latest viscosity map result in the primary version and giving me helpful suggestions. I thank Dr. Graham Potts and Prof. Zhenhong Li for critical and helpful reviews. I must thank my friend, Yujie Zhang for looking after my spirits and health. Finally, thanks to my family for their financial support and spirits support.

Declaration

I, *Jing Zhang*, confirm that the work submitted in this dissertation is my own, and that appropriate credit has been given where reference is made to the work of others.

Signature: Jing Zhang

Date:09/01/2015

Abstract

Western Mongolia is a seismically active intracontinental region, with ongoing tectonic activity and widespread volcanism attributed to the India-Eurasia collision. During the last century, four M > 8 earthquakes have occurred in Mongolia, which provides opportunities to study how continents deform. The 1957 Gobi-Altai earthquake is one of the largest magnitude earthquakes. The rupture pattern associated with this earthquake is complex, involving left-lateral strike-slip and reverse dip-slip faulting on several distinct geological structures in a 264 × 40 km wide zone.

To understand the relationship between observed postseismic surface deformation and the rheological structure of the upper lithosphere, Interferometric Synthetic Aperture Radar (InSAR) data was used to study the 1957 earthquake in southwest of Mongolia and model the late postseismic deformation. SAR data were acquired from the ERS1/2 and Envisat from 1996 to 2010. Using the Repeat Orbit Interferometry Package (ROI_PAC), 124 postseismic interferograms have been produced on four adjacent tracks. Stacking these interferograms yields a maximum InSAR line-of-sight deformation rate along the fault of < 6 mm/yr. Modelled surface deformation suggests that the viscoelastic relaxation is the most reasonable mechanism to explain the observed surface motion.

The main findings: (1) The maximum InSAR line-of-sight deformation velocity along the Gobi-Altai fault is about 6 mm/yr; and (2) Modelled surface deformation suggests that the viscoelastic relaxation is the most reasonable mechanism to explain the observed surface motion; (3) The optimal model cover the Gobi-Altai seismogenic thickness is 10 km; (4) the lower bound of Maxwell viscosity of lower crust and upper mantle is approximately 9×10^{19} Pa s, and the Maxwell relaxation time corresponding to this viscosity is 95.13 years.

Contents

List of Figures

List of Tables

Chapter 1

Introduction

The 1957 December 4 Gobi-Altai Mw8.1 earthquake is one of the great earthquakes to have occurred anywhere in the world. This event locates in the southwest of Mongolia, which is a NNE-SSW compression zone due to the India-Asia collision (Tapponnier and Molnar 1979; Cunningham 1998, 2005; Vassallo et al., 2007a). The deformation is a primary left-lateral strike-slip with north-south shortening along the east-trending Gobi-Altai mountain range. East-west shortening and reverse faulting also occurs in this area and was associated with the simultaneous rupture of several faults, such as Dalan Turuu, Hetsuu forebergs, Gurvan Bulag thrust and Toromhon Overthrust Kurushin et al. (1997). The Gobi-Altai region provides suitable conditions for remote sensing techniques such as Interferometric Synthetic Aperture Radar (InSAR) because of the arid climate, sparse vegetation and limited human modification of the surface (e.g., agriculture). These natural conditions also preserve the surface rupture of the 1957 earthquake for optical observation. In this study, I use geodetic observation to study the Gobi-Altai fault, including a high-resolution postseismic ground displacement dataset, a combination of remote-sensing datasets from Landsat images, and a detailed field map from Kurushin et al. (1997). Our aim is to identify the rheological structure of the lithosphere and upper mantle in the Gobi-Altai area by means of measuring the postseismic surface deformation after the 1957 event.

1.1 Motivation and aims

Mongolia represents the northernmost expression of the India-Asia collision deformation, and is considered to be the most seismically active area of the last century (Khil'ko et al., 1985; Baljinnyam et al., 1993). Six earthquakes with a magnitude of 7 or greater occurred in Mongolia. They are mainly concentrated on four major fault systems, which extend for several hundred kilometres. These strike-slip faults are potential fragile zones to come about large-magnitude earthquakes (Walker et al., 2007). The M 7.9 July 9th 1905 Tsetserleg earthquake is a left lateral strike-slip fault dipping to the northwest, with a reverse dip-slip component (Okal, 1976). The M 8.4 July 23rd 1905 Bolnay earthquake occurred on the southern branch of the major Bolnay fault (Calais et al., 2002). The M_s 8.0 August 10th 1931 Fu Yun earthquake rupture a 180 km long right-lateral strike-slip fault (Baljinnyam et al., 1993). The M_w 8.1 December 4th 1957 Gobi-Altai earthquake happened on the Bogd fault, it is an east-west trending left-lateral strike-slip fault (Kurushin et al., 1997). The M 7.1 1967 Mogod earthquake was located to the east of the Gobi-Altai fault, on a north-south striking mainly right-lateral rupture (Bayasgalan et al., 1999). Finally, the largest recent earthquake in this region was the Mw 7.2 event of 27th September 2003 in the Russian Altai mountains, with a right-lateral nodal plane striking parallel to a prominent fault-bounded valley trending WNW-ESE (Barbot et al., 2008).

This series of large earthquakes is closely associated with large-scale strike-slip faults, and provide opportunities to investigate how continents deform. The heated debate about the nature of tectonically-active continents is whether they deform by rigid block motion or more distributed process (continuum model). Many recent tectonic models of intercontinental deformation concern the behaviour of the lower continental crust (Burov and Watts, 2006; Freed and Bürgmann, 2004; Freed et al., 2006b; Hearn et al., 2002; Pollitz, 2003; Ryder et

al., 2007, 2011). The two end-member models try to explain the geological and geophysical characteristics of the Tibetan Plateau, as well as the forces that drive the deformation of the upper crust. The rigid body models imply that the major block-bounding strike-slip faults penetrate the entire thickened crust and extend down to the mantle. The crust behaves as a rigid or rigid-plastic cohesive unit under the rigid body condition (e.g., Leloup and Kienast, 1993; Rolland and Pêcher, 2001; Lacassin et al., 2004b; Valli et al., 2007, 2008; Rolland et al., 2008). In contrast, the continuum models consider a lithosphere with a Newtonian or power-law rheology, in which deformation is distributed throughout a continuously-deforming lithosphere, with the brittle upper-crustal discontinuities being much less significant (e.g., England and McKenzie, 1982, 1983; England and Houseman, 1985; Houseman and England, 1986). Geologists are not able to address this debate without a thorough understanding of plate dynamics. In addition, the rheological structure of the lithosphere plays a crucial role in the earthquake cycle because the rheology and movements of the lower crust and upper mantle movement influence fault activity over time.

It is well known that the rheological structure in northern and southern Tibet have significant differences (Molnar et al., 1973; Molnar and Tapponnier, 1975; Thatcher, 2003; England and Molnar, 2005), but the rheology of Mongolia investigations are still limited. Mongolia is regarded as remotely affected by India-Eurasia convergence. However, actual upper layer thickness and viscosity values for a particular region are commonly poorly-resolved; and only a few studies have investigated Mongolia rheology (Wright et al., 2013). Calais et al. (2003) use GPS geodetic measurements to derive a consistent velocity field for Asia, and have reported that westernmost Mongolia is shortening north-south, but in central and eastern Mongolia, the motion is eastward to southeastward with left-lateral shear. The Gobi-Altai fault is an E-W trending structure located in the southwest of Mongolia. Ritz et al. (1995)

based on in-situ-produced ^{10}Be technique to calculate minimum ages for alluvial surfaces misaligned and measured maximum slip rate of ~1.2 mm/yr. This slip rate is in agreement with Calais et al. (2003) who using GPS measurements in Mongolia between 1994 and 2002. Extension across the Baikal rift zone, north of Mongolia, is about 4 mm/yr (Calais et al., 2003). The most recent study on the Baikal area was by Barbot et al. (2008). They combined Envisat Advanced Synthetic Aperture Radar data and SPOT optical imagery to measure coseismic and postseismic deformation for the Mw 7.2 Altai earthquake (27th September 2003). They believe that the observed deformation is not able to explain by linear viscoelastic relaxation in the upper mantle or lower crust, constraining the dynamic viscosity of the lower crust to be > 10^{19} Pa s (Barbot et al., 2008). Vergnolle et al. (2003) also use GPS measurements to determine the viscosity of the lower crust and upper mantle. They established a viscoelastic two-layer model on a spherical Earth, with the upper layer representing the upper crust and with the lower layer depicting the lower crust and upper mantle. Ultimately, they find an upper mantle viscosity between 1 ×10^{18} and 4×10^{18} Pa s, and a weaker lower crust (3×10^{16} to 2×10^{17}) in the Baikal-Mongolia area (Vergnolle et al., 2003). They also claim that the 1905 Bolnay-Tsetserleg sequence and 1957 Bogd earthquake are the dominant contributions to the observed postseismic deformation.

The Global Positioning System (GPS) is a satellite-based navigation system, which have the ability to pinpoint the user's location anywhere on Earth (Federal Aviation Administration). Geodetic techniques such as InSAR and GPS provide valuable methods to quantify continental deformation on a large scale (McClusky, 2000). These techniques have been used for studying postseismic deformation and inferring lithospheric rheology (e.g., Nur and Mavko, 1974; Savage and Prescott, 1978; Thatcher et al., 1980; Thatcher and Rundle, 1984; Hetland and Hager, 2006; Johnson et al., 2007; Ryder 2007, 2014; Takeuchi and Fialko,

2012; Vaghri and Hearn, 2012; Yamasaki et al., 2013). It is now recognized that postseismic motion can be caused by some combination of any or all of the following processes: (1) transient aseismic fault slip ("afterslip"); (2) poroelastic relaxation due to fluid flow in the upper crust; (3) viscoelastic relaxation in the lower crust and/or upper mantle. Based on InSAR data, the kinematics of continental deformation can be simulated using computational and numerical rheological models, in order to constrain the viscosity of the continental lithosphere.

Gourmelen and Amelung (2005) combined InSAR with Global Positioning System (GPS) space geodetic techniques in order to measure late-stage postseismic transients deformations following large earthquakes in the Central Nevada seismic belt by averaging independent interferograms. Through model simulations, they infer that the deformation is caused by flow in the mantle underlying an elastic crust. The results of a comparable study on the 1957 Gobi-Altai historic earthquake that used a similar method (Gourmelen and Amelung, 2005) are reported in this thesis. A ground velocity map along the Gobi-Altai fault in radar line-of-sight direction are generated. The study focuses on the transient deformation after 38 years following the 1957 Gobi-Altai earthquake Mw 8.1, and it provides constraints on the rheology of the crust and upper mantle in the Gobi-Altai region. By evaluating the transient deformation of the postseismic motion, the response of the lithosphere to large earthquakes may be evaluated. This research aims to: (1) develop an InSAR dataset of postseismic deformation four decades after the 1957 earthquake, then derive a postseismic model in a spherical, radially layered elastic-viscoelastic Earth based on InSAR results; and (2) constrain the crustal viscosity in the lower crust and upper mantle using numerical modeling (VISCO1D) for this area; and (3) analyze the dominate contribution to the surface deformation. Studying this earthquake in western Mongolia is not only important for

understanding regional tectonics, but also for understanding the structure and dynamics of the lithosphere (e.g., Jackson and White, 1989; Chen et al., 2004; Elliott et al., 2010b).

1.2 The research questions

It is widely accepted that the high elevation of the Tibetan plateau is caused by crustal thickening in response to the collision of the Asia and Indian plates beginning 45 – 55 Myr ago (Owens et al., 1997). Strong evidence indicates that crust thickening, partial melting, and perhaps the lower-crustal flow happen under the Tibetan Plateau (Owens et al., 1997). Two opposite views of the deformation of Asia lead to the debate about how continents deform. The 'block motion' model regards continental deformation as entirely edge-driven, with the crust being fractured into several tectonic blocks separated by large-scale strike-slip faults (Tapponnier et al., 1982; Peltzer and Tapponnier, 1988; Avouac and Tapponnier, 1993; Replumaz and Tapponnier, 2003). In contrast, 'viscous sheet' models assume that the lithosphere can be considered as a continuous viscous medium (England and Molnar, 1997b; Flesch et al., 2001; Royden et al., 1997). In these models, India-Eurasia convergence is accommodated by crustal thickening, which induces lateral variations in gravitational potential energy that drives the present-day deformation. Analysis of the Tibetan Plateau strain rates yields an estimate of 10^{22} Pa s (England et al., 1997) for the average viscosity of the lithosphere, which is approximately 10 to 100 times greater than the viscosity of the convecting upper mantle (England et al., 1997). From this estimate, England and Molnar (1997) infer that the continents behave as continuously deforming solids.

Postseismic motion is manifest as transient slow creep in response to coseismic slip following an earthquake (from days to decades) (Ryder et al., 2007). Geodetic observation is suitable for recording this postseismic mechanical response (Ryder et al., 2014; Wen et al., 2012).

Resulting inferences of rheology provide valuable information in geodynamics and the earthquake cycle in the Gobi-Altai area. Observable surface displacements can be used to constrain the rheological properties of rocks and faults deep beneath the surface (Bürgmann and Dresen, 2008). Compared with other seismically active regions, the Gobi-Altai is still relatively unstudied. Barruol et al. (2008) use teleseismic shear waves (e.g., SKS phases) to investigate deep mantle deformation and find the Gobi-Altai fault remain largely undetermined deformation at depth. Windley and Allen (1993) reports that the Hangay Dome in central Mongolia is likely overlies a juvenile mantle plume, which makes the interpretation for localised movement in depth along surrounding area much harder. In this study, by using InSAR measurements, an analysis of how active faulting in Mongolia will be used to provide information about the rheology of crust and upper mantle. This information can be used to answer the following questions:

(1) What is the seismogenic thickness of the Gobi-Altai fault?

(2) What is the viscosity beneath the Gobi-Altai fault?

(3) Is the late postseismic phase dominated by viscoelastic relaxation, afterslip, or interseismic slip?

(4) Although the main Gobi-Altai fault is dominantly a left lateral strike-slip fault, it also includes several thrust fault segments in the system. This leads to a further question: What is the extent of strike-slip faulting, and how is it connected to thrust faulting?

1.3 Current postseismic research on rheological structure of the lithosphere

The Earth's mantle is a viscoelastic material (Thatcher and Pollitz, 2008). It flows like a very viscous fluid on long time scales. Large magnitude earthquakes change the stresses in the crust and upper mantle. Aseismic transient deformation occurs following major earthquakes. Observations indicate that postseismic displacements are normally an order of magnitude smaller than coseismic displacements and they have longer spatial wavelengths, and that the rate of displacement decreases with time over a period of years following the earthquake (Ryder et al., 2014). Eventually, the postseismic deformation decays to a steady state background interseismic deformation (Thatcher and Rundle, 1979). Several theories are given to explain postseismic observations: localised afterslip on a discrete fault plane (e.g., Marone et al., 1991; Bürgmann et al., 2002), slow creep in a viscous or viscoelastic shear zone (e.g., Hearn et al., 2002), distributed viscoelastic relaxation (e.g., Pollitz et al., 2000) and poroelastic rebound (e.g., Peltzer et al., 1998; Jónsson et al., 2003). It is hard to separate the different mechanisms for a strike-slip fault by geodetic observation because each mechanism is capable of producing similar observable surface displacements, and two or more processes may operate in each case study (e.g., Fialko, 2004; Freed et al., 2006a; Biggs et al., 2009;Ryder et al., 2007). Strike-slip zones become ductile shear zones in depth, and they play a fundamental role in lower crustal flow producing vertical foliations and horizontal stretching lineations (e.g., the San Andreas Fault)(Schulmann et al., 2003).

Since the early 1990s, satellite geodesy has been applied to investigating postseismic motion following several large strike-slip faults all over the world. For example, Landers in 1992 (e.g., Massonnet et al., 1994; Peltzer et al., 1996), Hector Mine in 1999 (e.g., Pollitz et al., 2001), Izmit in 1999 (e.g., Bürgmann et al., 2002), Denali in 2002 (Pollitz, 2005) and Manyi in 1997 (Ryder et al., 2006). Through observing surface displacements with a good spatial

and temporal resolution over days to decades following the earthquake, and by comparing the InSAR dataset with simulated datasets, we are able to infer the rheology of crust and upper mantle, which may give insight into the earthquake cycle. It is crucial that observations made at the late-stage of earthquake cycle in confining the viscosity of the upper mantle (Hearn et al., 2009). It is also a challenge to closely constrain the optimal upper bound on viscosity because the postseismic transient magnitude decreases with time (Bürgmann et al., 2013).

For the 1957 Gobi-Altai earthquake, the deformation caused by viscoelastic relaxation, afterslip and interseismic deformation are investigated separately. Afterslip is taken into account because it is possible that the slow slip happened at the locking depth 38 years after the earthquake (Kelin et al., 2012).

Earthquake pore pressure gradients cause poroelastic rebound. Flow to re-equilibrate pore pressure results in surface deformation. The dissipation of pore fluid pressure gradients is thought to occur only in the few years following an event (Peltzer et al., 1996b). Therefore, poroelastic rebound is unlikely to contribute to the deformation examined in this study, and no attempt was made to model this process.

1.4 Overview of the thesis

In this study, a set of interferometric data covering the whole 1957 Gobi-Altai earthquake rupture is compared with a number of computational models. In Chapter 2, the fault trace is identified using published field mapping, InSAR results and Landsat optical images. The InSAR dataset of surface deformation covering 38-53 years after the earthquake is presented in Chapter 3 together with description of methods used to remove topographic noise and correct orbital error. Chapter 4 presents the viscoelastic relaxation modeling using VISCO1D

software. It also contains afterslip modeling and interseismic modeling using disloc3d (Okada, 1985). In the Discussion (Chapter 5), the InSAR data is compared with the different models in order to link postseismic deformation with rheological properties of the crust and upper mantle. Possible explanations for the surface deformation observed by InSAR such as long-lasting afterslip and interseismic are discussed. The final chapter is the main findings of this study in the Gobi-Altai region.

Chapter 2

The Gobi-Altai fault and the 1957 Earthquake

2.1 Tectonic setting in Mongolia

Figure 1. Topography and main tectonic structures in Asia. Red rectangular is the study area Gobi-Altai fault. Picture are modified from CEOATLAS Graphi-Ogre

It is well known that crustal shortening accommodates most of India's penetration into Eurasia of about 2000 km at a rate of 50 mm/yr at the southern margin of the Himalaya arc (Molnar and Tapponnier, 1978). The effects of the Indo-Eurasian collision have been claimed to extend across and produced the late Cenozoic uplift of the Tibetan Plateau, Kun Lun, Qilian Shan, Tien Shan and Altai. From south to north across the Tibetan Plateau, the primary sutures are Indus-Tsangpo, Bangong, and Jinsha. Large strike-slip faults which including the Kunlun, Qilian and Gobi-Altai and compressional mountain ranges (Himalayas,

Pamir-TianShan, Mongolian Altai, Gobi-Altai) are presented (Tapponnier et al., 2003; Clark and Royden, 2000). The Tibetan and Mongolia plateaus have average heights of 5000 and 2500 m and crustal thicknesses up to 70 and 50 km respectively. The origin of the high elevation within continental interiors is still an open question in geodynamics. In June 2012, a temporary workshop (Stachnik et al., 2014) studied the crustal and upper mantle structure of the Hangay Dome in central Mongolia. H-k stacking is a method that estimates the average thickness and Poisson's ratio of the crust (Hazarika et al., 2013). Hangay Dome states north of Gobi-Altai, which is a broad regional uplift, the crust thickness measured from H-k stacking of receiver functions range from 42 km to 57 km, with thicker crust beneath the highest topography, the average Vp/Vs is 1.77 (Stachnik et al., 2014).

The Altai can be divided into two kinematically distinct mountain belts that meet at 46°N, 96°E: the right-lateral transpressive western Altai and the left-lateral transpressive Gobi-Altai (Cunningham, 1998). The Gobi-Altai is an intraplate, intercontinental transpressional orogen in southwest Mongolia that formed in the Late Cenozoic (Cunningham et al., 2005). The Gobi-Altai represents the northernmost active compressional belt in central Asia and uplift of an ancient peneplain that had formed during Jurassic time (Jolivet et al., 2007). The wide variety of tectonic phenomena creates major continental strike-slip faults.

In the eastern part of Mongolia lies the Baikal rift zone, which according to several studies, it is currently opening at 4-5mm/yr in a NW-SE direction (e.g., Calais et al., 2002; Vergnolle et al., 2003). The GPS velocity field in the Baikal Mongolia area can be considered to be a 3-5 mm/yr shear velocity gradient between the Siberian platform to the north and northern China to the south, as well as a contribution from postseismic deformation of about 2 mm/yr

following the 1905 Bolnay-Tsetserleg sequence and the recent 1957 Bogd earthquake (Vergnolle et al., 2003).

The 1957 Gobi-Altai event occurred on the Bogd fault of southwest Mongolia. The rupture of the entire fault reached to 270 km, and the maximum horizontal displacement was 8.85 m (Florensov and Solonenko, 1965). This earthquake also ruptured the Toromhon overthrust 30 km south of the main fault. The 23 largest aftershocks follow the general trend of the surface break within a zone 300 km long (Chen et al., 1973). Thrust faulting occurs in the Barkol Tagh, Karlik Tagh, and western Gobi-Altai Mountains (Figure 2.). The high-angle thrust faults that follow the northern foothills of Barkol Tagh and Karlik Tagh are perhaps the clearest examples of such faulting to be observed on the Landsat imagery of the central Asia. For example, the Dalan Turuu Foreberg located to the north of the Ih Bogd fault, whose displacement is 2 m (Florensov and Solonenko, 1965). Florensov and Solonenko (1965) described a northeast-southwest trending fault break with up to 9 m of vertical displacement. Tapponnier and Monlar (1979) define the primary fault scarp dipping to the east, toward the down thrown block.

18 different fault segments published by Kurushin et al. (1997) are modeled in this study. The segments from west to east are: the Bayan Tsagaan, Bahar, Noyon, Dalan Turuu Foreberg, Ih Bogd, Gurvan Bulag Rupture, TsagganOvoo-Tevsh Uul Rupture, the Hetsuu foreberg and Baga Bogd rupture. The detailed fault parameters are listed in Table 1.

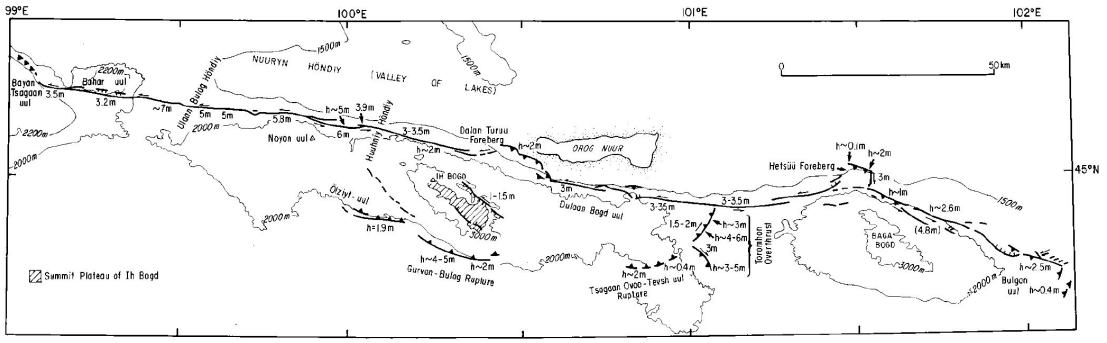

Figure 2. Summary of 1957 rupture, from Bayarsayhan et al. (1996). Dark black lines refers to the major strike-slip characterizes main east-southeast-trending zone north of Noyon uul, Ih Bogd, and Baga Bogd. Teeth indicate reverse or thrust faulting (h is the field measured vertical components of slip). Normal slip presented as tics.

2.2 Determination of the Fault Location

One month after the Gobi-Altai earthquake, a team of Russian and Mongolian geologists began to study the rupture (Florensov and Solonenko, 1965). Ultimately, they presented the classic monograph of the fault. Reconstruction of the fault trace was performed using a field map (Kurushin et al., 1997) displaying the major rupture along the principle Gobi-Altai fault.

The fault location used in this study was taken from this published field map (Kurushin et al., 1997). Photographs of the map were taken along the fault. ArcGIS10 was used to georeference each photograph in terms of the map's coordinate system information marked in the margins. Each photograph was referenced using four or five control point. The WGS-84 projection was chosen so that the field map fit with the controlled map. A character layer was created, and the fault trace was digitised manually and saved as a document file. The digitised file contains each point of the fault trace in latitude and longitude format. The fault trace

coordinates were used into Matlab to show the location of the fault and enable comparisons with InSAR results and viscoelastic modelling.

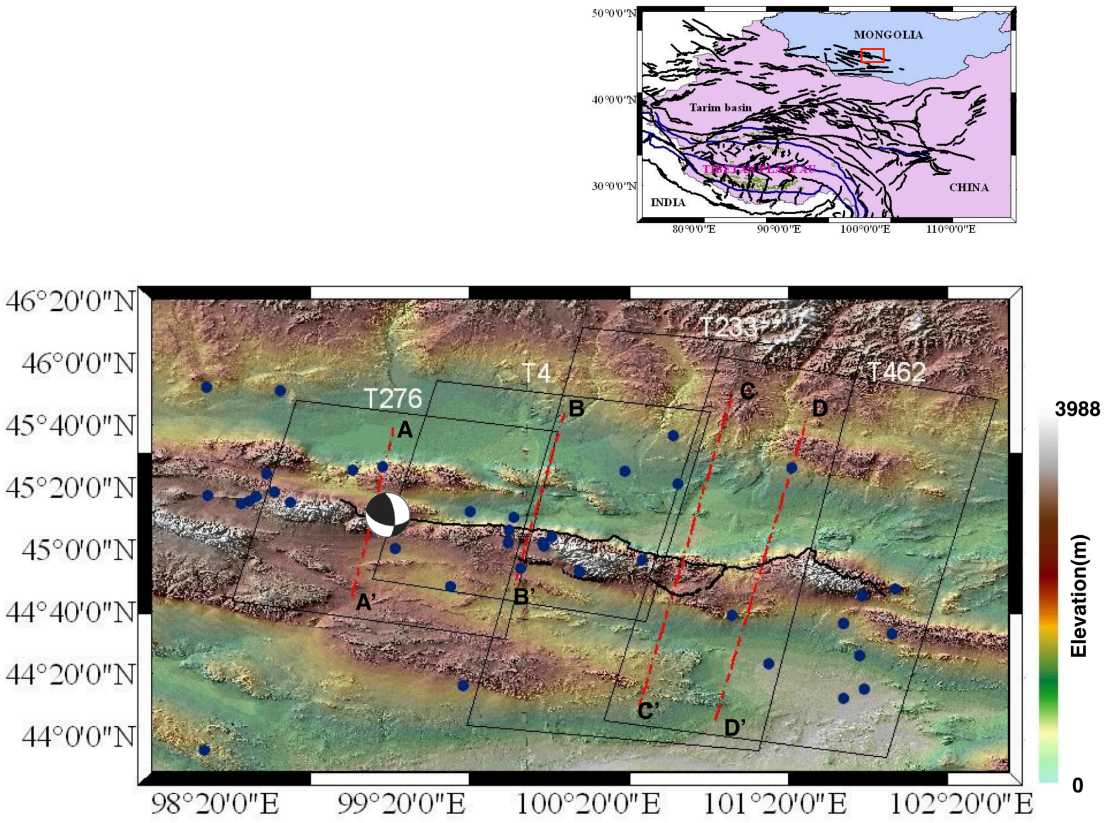

Figure 3. Shaded relief topography of the Gobi-Altai Fault in south Mongolia. DEM is 90 m SRTM. Fault trace is shown in thick black line, and focal mechanism is taken from Bayasgalan et al. (1999). Dark blue dots mark locations of earthquakes with Mw > 3 (from USGS and ANSS catalogue between 1957 and 2011). Numbers above black boxes mean SAR tracks. A-A', B-B', C-C', D-D' denote locations of displacement profiles shown in Figure 20.

2.3 Seismology

For the 1957 December 4th earthquake, the location was recorded by several seismological studies (Chen et al., 1977; Florensov and Solonenko, 1965; Molnar and Deng, 1984). The

main shock was located at latitude 45.15°N, longitude 99.20°E, based on surface ruptures (270 km long, 20 km width, and coseismic slip of 8 m), the moment magnitude are defined at M_w 8.1 (Molnar and Deng, 1984). Kurushin et al. (1997) using their field map estimate the moment magnitude at M_w 7.8~7.9. Chen et al. (1977) find latitude 45.31°N, longitude 99.21°E. The USGS catalog records the location as 45.31°N, longitude 99.21°E, with M_w 8.1. The seismic moment is 1.3×10^{28} dyn-cm (Chen et al., 1977), 1.76×10^{21} Nm (Okal, 1976), which is equivalent to a M_w 8.1 earthquake. Rizza et al. (2011) using fault parameters from Kurushin et al. (1997), they estimate the moment magnitude of the Gobi-Altai earthquake at M_w 7.78-7.95. From seismic waves, the moment magnitude had been estimated between M_w 8.0 and M_w 8.3 (Pacheco and Sykes, 1992).

Due to the complex surface faulting of the Gobi-Altai fault, the work of Kurushin et al. (1997) was used to constrain the parameters that were input into the viscoelastic relaxation, afterslip, and interseismic models. Most studies define the length of the fault as 264 to 270 km, and the depth of the Gobi-Altai earthquake epicenter as 20 km (Vergnolle et al., 2003; Pollitz, 2003). In this study, a fault depth of 15 km was used in the viscoelastic relaxation model. This depth is chosen because it is the depth which most distribution of earthquakes in this area with this depth (Déverchère et al., 2001)

Table 1. Focal Mechanism Solutions of 1957 December 4th Gobi-Altai earthquake

Earthquake	Strike	Dip	Rake	Top(km)	Bottom(km)	Magnitude	Reference
Study1	103	53	32	0	-	Mw8.1	Okal (1976) (Molnar and Deng, 1984)
Study 2	101	70	9	0	-	Mw8.1	Kurushin et al. (1997)
Study 3	103	53	90	0	20	Mw8.1	Pollitz et al. (2003)
Study 4	101.4	70	9	0	20	Mw8.1	Vergnolle et al. (2003)
This Study	101.4	53	9	0	15	Mw8.1	

Table 2. Summary of Displacement Along the 1957 Surface Rupture (Kurushin et al., 1997).

Fault segment	Lat. (°N)	Long. (°E)	Strike (°)	Dip (°)	Rake (°)	Length (km)	Displacement (m)	Rupture
1	45.17	99.25	100	90	0	37	3.2	Bogd, west end
2	45.12	99.71	99	90	0	45	6.0	Bogd, Ulaan bulag to Öndgön Hayrhan
3	45.08	100.06	97	90	0	9	3.5	Bogd, near the Hüühniy höndiy
4	45.04	100.36	106	77	30	41	3.5	Bogd, north-northeast of Ih Bogd
5	44.96	100.90	100	90	0	44	3.5	Bogd, from Dulaan Türüü to east of the Toromhon Overthrust
6	44.95	101.38	75	90	0	30	3.5	Bogd, northwest of Baga Bogd
7	44.92	101.73	115	60	33	40	5.0	Bogd, northeast of Baga Bogd
8	44.75	102.02	100	45	90	11	3.0	Bogd, north of Bulgan uul (thrust slip)
9	44.84	102.04	75	90	0	7	0.5	Bogd, north of Bulgan uul (strike slip)
10	44.78	102.09	0	45	90	8	2.0	Bogd, east end
11	44.80	101.03	216	45	110	12	5.0	Toromhon Overthrust, northern portion
12	44.82	101.01	180	45	90	5	0.3	Toromhon Overthrust, southern portion
13	44.85	100.92	240	45	90	7	1.5	Tsagaan Ovoo-Tevsh uul, eastern portion
14	44.83	100.85	273	45	74	9	3.0	Tsagaan Ovoo-Tevsh uul, central portion
15	44.86	100.73	300	45	90	10	1.0	Tsagaan Ovoo-Tevsh uul, western portion
16	44.82	100.33	278	45	90	25	4.0	Gurvan Bulag
17	44.93	100.08	286	45	90	18	3.0	Ölziyt uul
18	44.93	100.45	134	90	0	30	2.0	Ih Bogd summit plateau

Orientations are defined by standard seismological conventions (e.g., Aki and Richards, 1980), and displacements are parallel to the slip vectors. (Kurushin et al., 1997). The latitude and longitude indicate the center of the fault trace of each fault segment.

2.4 Locating the Fault Trace with Landsat Imagery

Remote sensing has been used in recent decades for mapping faults in different parts of the world. Remote sensing data allow the detection of structural features and offer opportunities for improving mapping and identifying the areas that are likely to be locations of earthquakes. Major fault traces were identified in Mongolia, the Tien Shan and the Himalaya (Tapponnier and Molnar, 1979) by combining satellite images and mapping active geomorphic features. In this study, digital image processing and visual interpretation were

used to delineate geological lineaments in this area. Two Landsat 7 ETM+ images (Path: 134, 135 Row: 29) were used in this study. They were acquired on 20/10/2000 and 20/03/2001 respectively (NASA Landsat Program).

Landsat 7 ETM+ images with scene size (185×185 km), pixel resolution 30 m were used in the combination of 741 (RGB) as the most suitable for defining the fault (Sevki et al., 2009). The ENVI 4.5 (Environment for Visualizing Images) software was used to stack the three bands of the Landsat images. This combination provides rich geological, lithological and surface environmental information. Structural features, different types of rocks, geological contacts and lithostratigraphic units can be interpreted on the false color image.

As can be seen in the Landsat image (Figure 4), geomorphic features can be traced over a length of approximately 270 km. Complex alluvial fan and splay fault traces indicate the position of the fault rupture. The correlation between 18 fault segments (Table 2) with the Landsat image can be considered in five parts: (1) the segments numbered 1 to 10 are the main left-lateral strike-slip components, marked in red line with two opposite arrows along the Bogd fault on the Landsat image; (2) the segments between 11 and 15 represent the Toromhon Overthrust and Tsagaan Ovoo-Tevsh uul reverse section, located at the middle bend of the main fault; (3) segment 16 stands for the Gurvan Bulag thrust on the south side of the Ih Bogd mountains; (4) number 17 indicates the Ölziyt uul thrust fault dipping to north; (5) number 18 refers to a short left-lateral strike slip fault on the summit of the plateau.

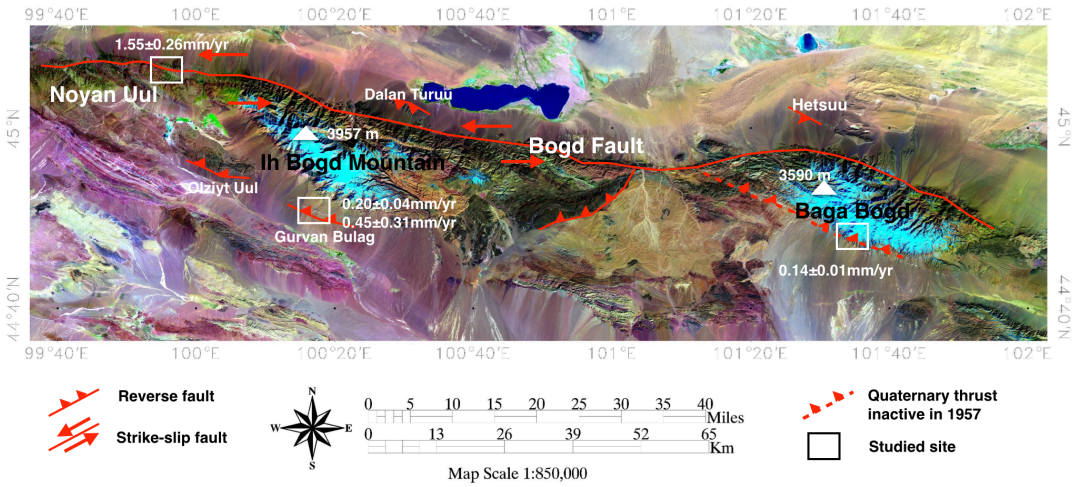

Figure 4. This false colour image uses Landsat ETM+ 7 (shortwave infrared) for red, band 4 (near infrared) for green, and band 1 (blue) for blue. Simplified tectonic map of Gobi-Altai fault (modified after Vassallo et al., 2007). Based on Landsat ETM+ 7 data provided by the NASA Landsat Program, 2000.

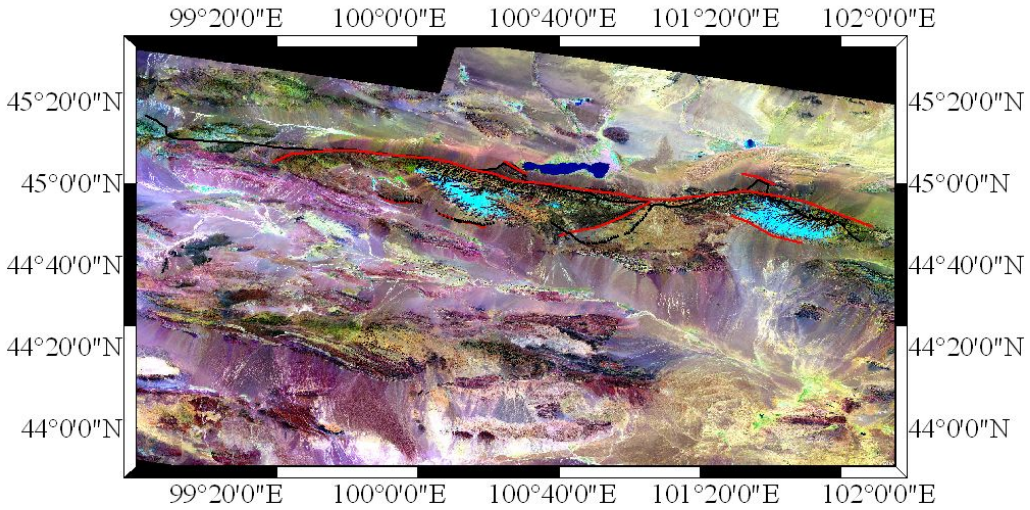

Figure 5. Two digitised fault traces from Kurushin et al. (1997) in black and Vassallo et al. (2007) in red, respectively.

In order to ensure the accuracy of the digitised fault trace from Kurushin et al. (1997), the 18 fault segments trace are overlaid with Landsat ETM+7 image

(Figure 5 in black line). The red line is the fault trace acquired from Vassallo et al. (2007) using Landsat visual interpretation. Comparisons are made between the two digitised Gobi-Altai fault datasets. As can be seen from the Figure 5., apart from slight discrepancy in the bend area at the middle of the Bogd fault, the digitised two dataset are in consistent in most of segments. It proves the digitised fault trace from Kurushin et al. (1997) is precise. This fault traces (black line) are used for InSAR observation and modelling interpretation later on.

Chapter 3

InSAR Observation

3.1 InSAR principle

Space-borne Interferometric Synthetic Aperture Radar (InSAR, also abbreviated as IFSAR or ISAR) is an advanced geodetic tool. SAR data have advantages including near global coverage and all-weather, day-night capability. This geodetic technique calculates the interference pattern caused by the change in phase between two SAR images acquired by spaceborne synthetic aperture radar at two distinct times on a pixel-by-pixel basis (Massonnet and Feigl, 1998). The resulting image, called an interferogram, is a map that records the variation in distance between the ground and the radar source during the time interval between the two observations. The direction between radar and the surface of Earth is usually referred to as line-of-sight direction. Therefore, InSAR provides highly detailed images of the amount of movement of the ground relative to a satellite. This technique is very useful for monitoring ground movements because of its exceptional spatial resolution (10 m) for C-band SAR data, and high measurement precision in millimetre.

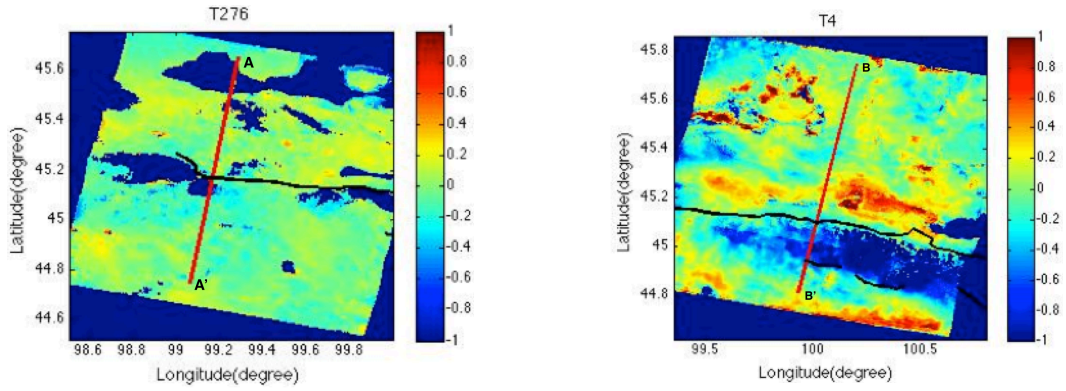

(a) (b)

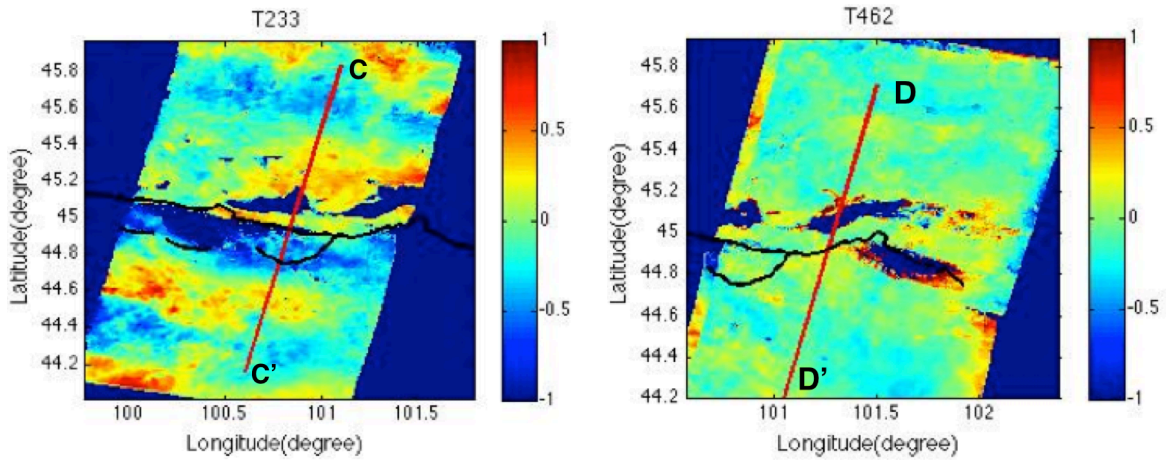

(c) (d)

Figure 6. Postseismic interferogram rate maps on four tracks shows separately. Colour scale is line-of-sight velocity in cm/yr. Black line shows 18-segment fault trace as mapped fieldwork (Kurushin et al., 1997). Red line A-A', B-B', C-C', D-D' denote locations of displacement profiles shown in Figure 20 a,b,c,d, a',b',c',d', and also show the elevation plot at the right side y axis. Positive range change refers to movement away from the satellite, negative range change refers to movement toward the satellite.

3.2 Radar image data sets for interferometry

Multiple SAR acquisitions from the ERS-1, ERS-2 and Envisat satellites spanning 1995 to 2010 were used to construct interferograms in this study. The line-of-sight incidence angle at the center of the image track is ~23° for ERS1/2 and Envisat. Interferogram images were generated from repeat-pass spaceborne synthetic aperture radar systems, on four satellite tracks (Tracks 276, 4, 233, 462). 124 postseismic interferograms were constructed, using the ROI_PAC processing software developed at Caltech/JPL (Rosen et al., 2004). All of the SAR data were from descending tracks. For the first two tracks (Track 276, Track 4), each interferogram uses only one frame (ERS-2, Frame 2694; Envisat, Frame 2693). For the last

two tracks (Track 233, Track 462), each interferogram was generated from two frames (2691, 2709). NASA's Shuttle Radar Topography Mission 90 m resolution digital elevation model (DEM) was used to remove topographic phase (Farr and Kobrick, 2000; Rodriguez et al., 2006). The DEM accuracy is ±16 m absolute and ±6m relative vertical accuracy depending on various regions (Rodriguez et al., 2006). Delft precise orbits are used in processing to eliminate orbital contributions. Coherence is excellent over the four tracks, probably due to the sparse vegetation and the arid climate. Even though the atmospheric noise level is not very high, for postseismic studies where the surface deformation is small, it can have an enormous impact on the interpretation of results. In addition, the Gobi-Altai fault lies along the edge of mountains, which gives rise to topography-correlated noise in the interferograms (Ryder et al., 2014).

15 years (1995-2010) of SAR data from the ERS and Envisat satellites was used to search for a postseismic signal from the major earthquake in 1957 on the Gobi-Altai left-lateral strike-slip fault, and no major earthquakes larger than M 7 happened after 1957. Since the data were acquired after five decades following the earthquake, the observed signal should solely be ascribed to viscoelastic relaxation, and not mixed with transient processes such as afterslip and poroelastic rebound (Ryder et al., 2014). However, recently published studies on other faults provide substantial evidence that afterslip may last for 30 years or even longer after the main shock (Copley, 2014; Wang et al., 2012). Therefore, an afterslip model was prepared for comparison with the InSAR data.

In order to increase the signal-to-noise ratio of the surface deformation and identify any late stage postseismic signal, stacking of interferograms was carried out (Sandwell and Price, 1998; Sandwell and Sichoix, 2000). The result shown in Figure 6 presents the average rate of

motion relative to the satellite in the line-of-sight direction. In this study, some interferograms with obvious contributions from atmospheric and topographic effects were excluded. These kinds of noise contaminate the final result in the stacking process. Additionally, interferograms with low coherence and disconnected phase were omitted.

In the process of interferogram processing, some individual patches can have k2π offsets (k is integer), so tie-point -- an unwrapping approach is used to manually chose positions and unwrap them based on a branch-cut method (ROI-PAC classic unwrapper) supported by Goldstein et al. (1988). The stacked result was compared with the output of viscoelastic relaxation, interseismic and afterslip models respectively. Running a range of viscoelastic relaxation, interseismic and afterslip models, this study trying to find the optimal explanation by calculating the minimum misfit between observations and models. Furthermore, understanding what is the reason caused the surface movement after the main shock.

As can be seen in Figure 6, the descending InSAR rate maps show average line-of-sight velocities from 1995 to 2010. A distinct broad blue-to-red transition can be seen across the fault, as expected for a long left-lateral strike-slip fault, which correspond to the north side of the fault move away from the satellite and south side of the fault move towards the satellite. On Tracks 4 and 233, the pattern of descending line of sight velocity consists of a lobe of positive range change to the north of the fault and a lobe of negative range change on the south of the fault, which is correspond to a left-lateral strike-slip mechanism.

But due to the complex landscape, several thrust and reverse rupture states near to the main Bogd fault. Assuming the north side Dalan Turuu thrust moves up, the InSAR rate map red signal will decrease in this part because the vertical movement counteract the phase due to

horizontal movement. On the contrary, if the active reverse components locate at the south side of the Gobi-Altai fault, these surface displacement rates will increase the negative range that are considered to be part of the left-lateral movement. The peak relative displacement occurs in the near field covered by Track 4 and Track 233 (at a distance of ~8 km on north side of the fault, ~ 25 km on south side of the fault), with a maximum of 6 mm/yr range change from peak-to-trough (Track 4 in Figure 6). This result is not very confident because the same tectonic signal does not show on overlap regions in both Track 4 and Track 233.

Compared to ascending tracks, descending tracks observe the deformation parallel to the fault, which is advantageous for measuring surface displacement. In addition, only several ascending scenes were available, with limited time span, so these were not used in this study.

3.3 Correction of tropostatic noise and orbital error

Five principal components are included in the original interferogram which record the phase, $\phi_{\Delta ti}$: (1) changes in the satellite orbits when the two SAR images were acquired, $\phi_{orb,\,\Delta ti}$; (2) topography-related phase change, $\phi_{topo,\,\Delta ti}$; (3) ground deformation, $\phi_{def,\,\Delta ti}$; (4) atmospheric propagation delays, $\phi_{atm,\,\Delta ti}$; and (5) random noise, $\phi_{noise,\,\Delta ti}$ (instrument drift and approximations in the processing software). These effects can be described as,

$$\phi_{\Delta ti} = \phi_{topo,\,\Delta ti} + \phi_{def,\,\Delta ti} + \phi_{atm,\,\Delta ti} + \phi_{orb,\,\Delta ti} + \phi_{noise,\,\Delta ti}; \qquad \text{(Equation 1)}$$

Knowledge of a satellite's position and altitude is required to remove the effect caused by the differences in the satellite orbit of the two passes. The atmospheric and topographic contribution contains most of the phase noise. Given that the postseismic deformation has a

low amplitude signal, suitable methods must be used to remove atmospheric and topographic noise which are of similar magnitude.

To minimize the negative effect of noise, before applying an algorithm to correct orbital error, topographic noise and atmospheric perturbation, I manually fix the small unwrapping errors as far as possible. A least square method was applied in each interferogram to remove a shift plane due to orbit error. G is the matrix of each uncorrected individual interferogram,

$Gm = d;$ (Equation 2)

$G = [x\ y\ 1];$

$m = \begin{bmatrix} a \\ b \\ c \end{bmatrix};$

$\phi_{orb,\ \Delta ti} = ax + by + c;$ (Equation 3)

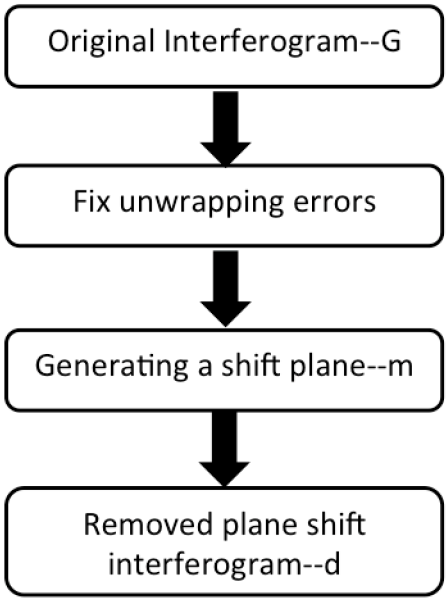

Figure 7. Simplified flow diagram to explain remove orbit noise.

x and y are range and azimuth coordinates, and a, b and c are constants for each interferogram that best fit the plane due to orbit error, d refers to the corrected phase for each interferogram. Starting with the original phase $\phi_{\Delta ti}$ and subtracting the orbit shift plane $\phi_{orb,\ \Delta ti.}$ from each individual interferogram, finally, the algorithm gives the orbit-corrected interferogram. Figure 8 is an example to present one of the interferograms before the orbit correction (a) and after (b).

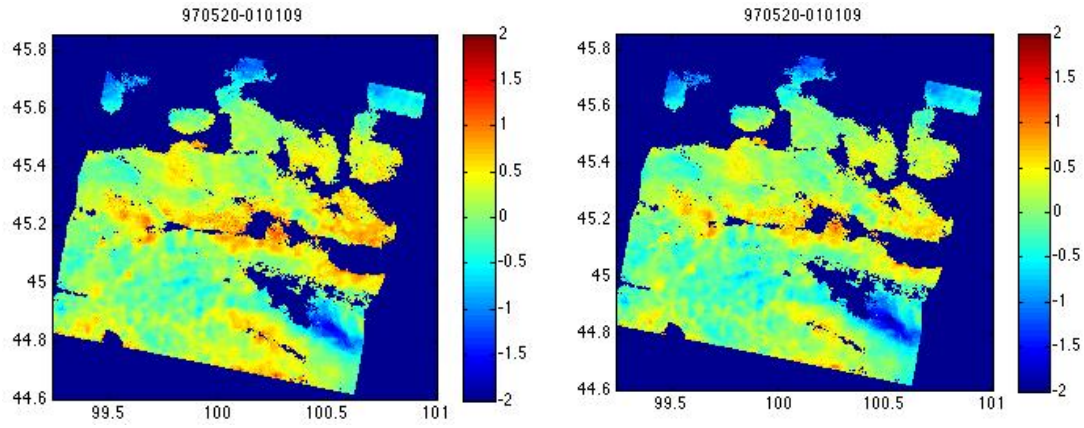

(a) (b)

Figure 8. Two interferogram images are in Track 4 (a) shows the interferogram before the orbit correction, (b) shows the same interferogram after orbit correction, with a decrease in noise. The title of the interferograms refers to the dates to form the interferogram. The colour scale are line-of-sight displacements in cm.

Atmospheric signal delays can produce substantial errors that contaminate the geodetic data. Tropospheric and ionospheric layers in the atmosphere are the two main reasons for radar echo delays. In this study the ionospheric propagation delay has been ignored because it only induces a relatively weak effect in ERS and Envisat C-band data (Gray et al., 2000). In order to mitigate noise in the long-term postseismic observations, some of the individual interferograms were removed from the stacking process when they contain significant atmospheric noise based on prior experience. In flat terrain, the vertically stratified water vapor delay is homogeneous (Cavalié et al., 2007). As for elevation changing area, the topographically-correlated atmospheric noise has a linear relationship between elevation and atmospheric delay (Cavalié et al., 2007).

An assumption was made that earthquake-induced displacements must decrease to zero at a finite distance from the fault. A modeled topographic noise algorithm (Rigo et al., 2004),

which aims to find a minimum constant, *k*, that makes the far-field displacement closest to zero was computed for each interferogram. Under this circumstance, calculating the water vapor amount between two SAR acquisitions and subtract the elevation-related phase from the whole interferogram (Cavalié et al., 2007). By way of example, Figure 9 shows a comparison between one of the interferograms before and after topographic noise removal.

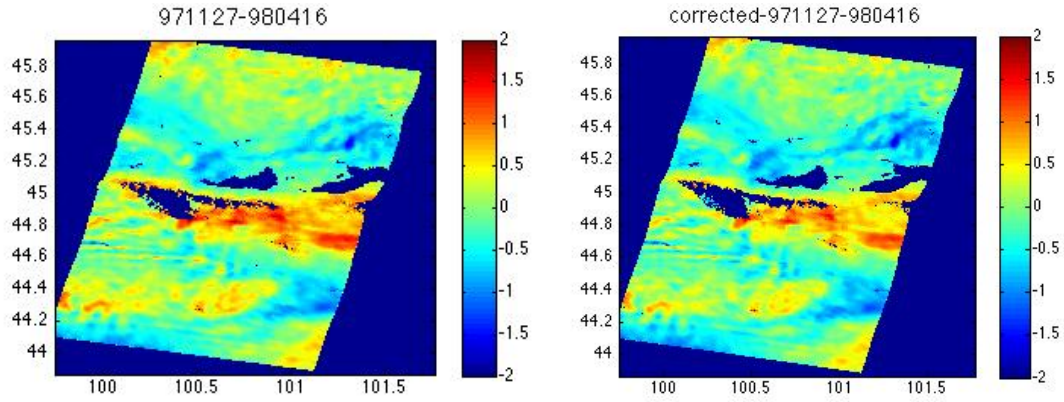

(a) (b)

Figure 9. Two interferogram images on Track 233. (a) Shows the interferogram before removing topographic noise, and (b) shows the same interferogram after topographic noise removal, with a slight change in the positive topographically-correlated noise. The title of the images refers to the SAR acquisition dates to form the interferogram. The colour scale shows LOS deformation in cm.

When I combine the topographic noise with previous orbit error estimation, the process can be written as a simple equation (Doin et al., 2009),

$\phi_{orb+topo,\,\Delta ti} = ax + by + c + d + kz$; (Equation 4)

where x and y are range and azimuth coordinates and z is the relative elevation of study area, and a, b, c and d are constants. This correction was performed on all of the interferograms for the four tracks.

In order to evaluate the accuracy of the InSAR observation, as well as assess the noise removing approaches. Comparisons between observations of adjacent tracks in common areas are performed.

3.4 Analysis of the InSAR rate map

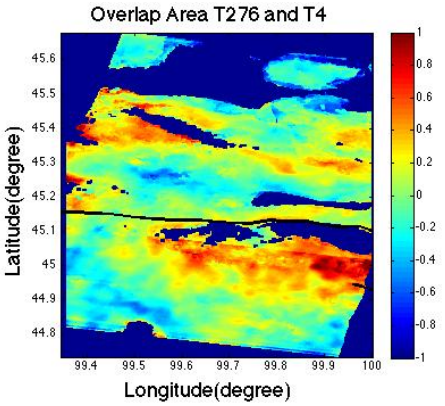

(a)

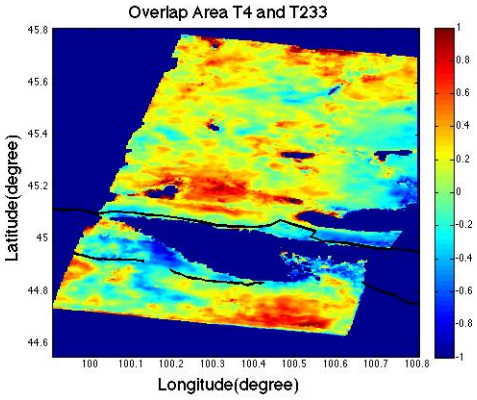

(b)

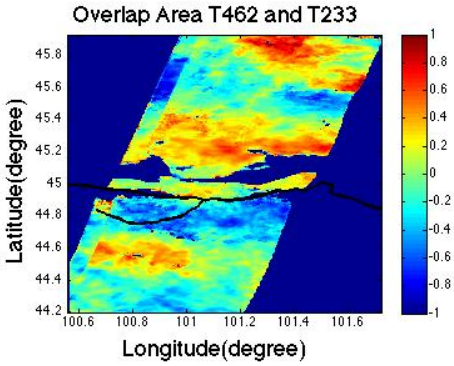

(c)

Figure 10. Overlap area along four adjacent tracks. Black line marks fault trace. (a) Track 276 minus Track 4; (b) Track 4 minus Track 233; (c) Track 233 minus Track 462. Colour scales show displacement rate in cm/yr.

One argument critical to the validity of this study is consistency of the InSAR rate map with the topography pattern, which needs to be resolved before accepting the InSAR result. The following evidence suggested that the observed signal represents a real tectonic signal.

Firstly, the interferograms formed from short time interval acquisitions do not show any similar signature with long time interval acquisition interferograms. Secondly, the reason why the discontinuities in the InSAR rate map are likely to be tectonic signal is that the red lobe located on the north side of the mountains, which indicate this region is move away from the satellite line-of-sight direction (Track 4). The broad positive displacement extends to a wide area towards the north (Figure 6), also indicate the surface displacement occurs in a broad area, which does not correspond to the localised elevation change. Furthermore, the dark green line in Figure 20 shows the elevation across the fault with the same location as InSAR deformation rate profiles. The movement rate map shows a distinct pattern different to the elevation variation. Therefore, the InSAR rate map signals are probably not derived primarily from topographically-related atmospheric noise. Thirdly, the maximum surface deformation on the velocity map is in agreement with the most of slip happened in the Gobi-Altai region (Rizza et al., 2011; Ritz et al., 1995). In short, these aspects of the signal imply that the discontinuities coincide with the trace of the fault movement. An attempt was made to confirm this result using adjacent overlapping areas between different tracks, correlation coefficients were calculated for the areas between successive SAR tracks.

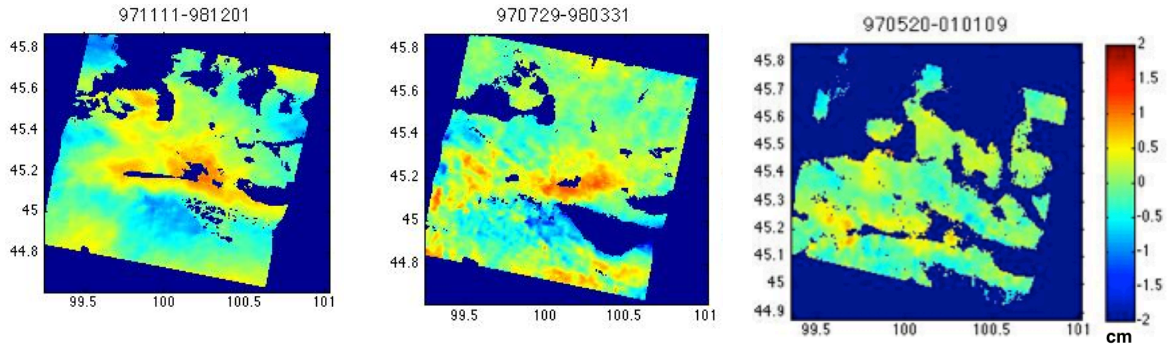

Figure 11. The three individual interferograms shown on Track 4 gives the similar pattern for the apparent tectonic signal in cm unit. But the third interferogram with longer time-span is expected to have more significant signal than the other two. This phenomenon

maybe an evidence for the interferograms includes both atmospheric noise and actual tectonic signal.

The correlation coefficient for Track 276 and Track 4 is 0.0821, which suggests that there is a weak relationship between the two datasets. For Track 4 and Track 233 the value is 0.5712, which illustrates that a moderate, positive correlation exists in the two datasets. Track 233 and Track 462 has a negative correlation (-0.0538). These values does not suggest that the overlapped InSAR results are strongly correlated, that is to say, the InSAR datasets includes an amount of noise. Further analysis on InSAR overlap regions can be seen in Appendix D. Decreasing the atmospheric and topographic noise in the datasets is crucial for any future work (see Chapter 6.2). In view of the noise contribution, histograms were made between each of the overlapping areas. The frequency histograms shown below (Figure 12, 13, 14) are near to normally distributed, with a mean very close to zero and standard deviations in the range 0.2908 cm/yr to 0.3273 cm/yr. The histogram in Figure 12~14 shows the distribution of discrepancies.

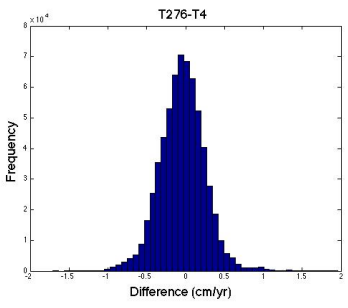

Figure 12.
Pixel differences between adjacent descending tracks 276 and 4, with a standard derivation of 0.2908cm/yr

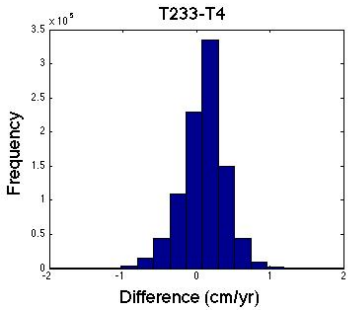

Figure 13.
Pixel differences between adjacent descending tracks 4 and 233, with a standard derivation of 0.3197 cm/yr

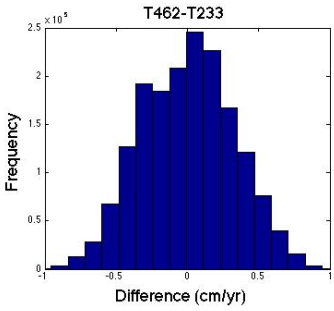

Figure 14.
Pixel differences between adjacent descending tracks 233 and 462, with a standard derivation of 0.3273 cm/yr

The processed InSAR four tracks data were used for the viscoelastic relaxation, afterslip, interseismic deformation modelling respectively in Chapter 4.

Chapter 4

Modelling

A three series of models were performed in order to understand the surface velocity obtained by InSAR. The three subsections below provide a quantitative investigation of a partial postseismic deformation mechanism. For modeling purposes, the three models -- viscoelastic stress relaxation; afterslip; interseismic deformation—are treated separately. Not only is each mechanism capable of inducing spatially similar displacement fields (Savage, 1990; Hearn, 2003), but also two or three of these mechanisms may operate at the same time. The aim is to determine whether the observed InSAR surface measurements can be explained by any one of the mechanism on its own or in combination. The InSAR dataset is modeled using the detailed fault parameters from Kurushin et al. (1997).

4.1 Viscoelastic Relaxation

4.1.1 Method

Earthquake-induced stress changes will trigger ductile flow in the lower crust and upper mantle that can lead to transient deformation at the Earth's surface. The viscosity in the lower crust or upper mantle controls the time constant of stress relaxation. Viscoelastic models of earthquakes can be restricted to a combination of elastic and viscous elements (Flugge, 1975). In Figure 15, springs represent elastic elements with shear modulus μ, whereas dashpots represent viscous elements with viscosity η. The earthquake stress relaxation behaviour can be expressed as a combination of two parts: (1) the stress relaxation response

σ(t) (constant strain rate); and (2) a creep relaxation response ε(t) (constant stress). But for various linear viscoelastic systems, different combinations of elastic and viscous elements can be easily generated based on the principle that σ(t) and ε(t) are functions of rigidity and viscosity (Ryder, 2006).

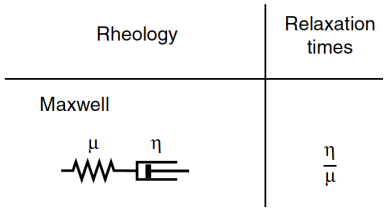

Figure 15. Maxwell rheology schematic illustration

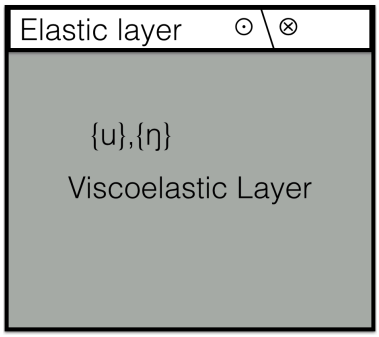

Figure 16. Simplified Maxwell body for a left-lateral strike slip fault. Lid over a viscoelastic half space case. Different models corresponding to increasing upper layer thickness (10 km, 15 km, 20 km, 30 km) and viscosity (1×10^{17} Pa s, 1×10^{18} Pa s, 1×10^{19} Pa s, 1×10^{20} Pa s, 1×10^{21} Pa s, 1×10^{22} Pa s, 1×10^{23} Pa s) were implemented. The elastic upper layer has shear modulus μ and the underlying layer has a viscous element with viscosity η.

A Maxwell material can be represented as a spring and dashpot in series as shown in Figure 15. The total strain rate is the sum of the strain rate in the spring and the dashpot. However, the force requires that the stress must be the same in each element (Segall et al., 2000), therefore:

$\dot{E}_{total} = \dot{E}_{spring} + \dot{E}_{dashpot}$; (Equation 5)

$= \frac{\dot{\sigma}}{2\mu} + \frac{\sigma}{2\eta}$,

This equation captures the material behavior where over short times, the material behaves elastically, but at long time scale, it behaves like a viscous fluid. Stress relaxation is governed by a single relaxation time, τ_M, defined as

$\tau_M = \frac{\eta}{\mu}$. (Equation 6)

4.1.2 VISCO1D

In order to investigate whether or not a simple viscoelastic layered model can replicate the observed movements, VISCO1D (Pollitz, 1992) code was used. VISCO1D uses a spherically stratified elastic-viscoelastic Earth model and computes the internal or surface displacements generated by an earthquake in a user-specified period. In this model, surface deformation is controlled by three sets of parameters: (1) the faults parameters (strike, dip, slip, rake, length, depth of upper and lower fault edges, and the latitude and longitude of one fault corner); (2) the relative thickness of the upper (elastic) crust layer and the lower (viscoelastic) layer, and; (3) the viscosity of the lower crust and upper mantle.

In the viscoelastic relaxation model, the chief Gobi-Altai fault includes 18 segments with various parameters based on Kurushin et al. (1997) and his colleague's field work. Due to the complex structure of the whole fault, the detailed descriptions of the fault segments (Table 2) were incorporated in the viscoelastic relaxation model to simulate the surface displacement using VISCO1D. In order to determine the elastic thickness of the crust and the viscosity of

the underlying substance, a two-layer Earth model consisting of an elastic plate overlying a viscoelastic half-space was constructed. According to Wright et al. (2013), the estimated seismogenic thickness globally is 14±5 km and 14±7 km from coseismic and interseismic observations respectively.

A test search was conducted with the top layer thickness ranging between 10, 15, 20, 30 km and the viscosity varying from 10^{17} to 10^{23} Pa s. For each combination of these two variables, a linear viscoelastic model was used to account for the postseismic deformation, and each fault segment represents one pattern of relaxation with its own decay time and spatial deformation pattern. Cumulative line-of-sight displacements since 1996 to 2010 were constructed in VISCO1D. When comparing to the InSAR rate maps, the accumulated displacements are then divided by the corresponding time interval.

Whilst a three-layer model with different viscosities for the upper mantle and lower crust would be more satisfactory because the low signal-to-noise ratio in the rate maps would make it difficult to resolve variations in viscosity with depth. But this study only concentrate on the Maxwell body rheology.

The root-mean-square (rms) misfit between the InSAR rate map and model is calculated according to

$$\chi^2 = \frac{1}{n}\sum_{i=1}^{n}[(d_i - m_i)^2], \qquad \text{(Equation 7)}$$

where χ^2 is the misfit squared, n is the number of points on the ground, and d_i , m_i are the line-of-sight displacements for the i^{th} point on the surface from the InSAR observation rate

map and viscoelastic relaxation displacement model, respectively (Ryder et al., 2007). Root – mean-square misfit calculations method have been used when searching for optimal viscoelastic and afterslip models in this study. The overall viscoelastic relaxation misfit is calculated for various elastic upper crustal thicknesses and viscosity separately (shown in Figure 17, Figure 18 respectively).

4.1.3 Maxwell rheology

In the process of modelling with a Maxwell rheology, the parameters varied are the upper layer thickness and the viscosity of the underlying viscoelastic half space. The shear modulus is held constant at 3×10^{10} Pa because the Gobi-Altai fault depth shallower than 20 km (Rizza et al., 2011). The aim is to compare modelled surface displacement velocities with velocities measured by InSAR and to calculate the misfit under each scenario.

The total misfit on four tracks value against increasing thickness of elastic upper layers (10 km, 15 km, 20 km, 30 km) is shown in Figure 17. Root-mean-square misfit values increase with greater upper layer thickness. The misfit curves as a function of viscosity with varied elastic upper layer thickness are shown in Figure 18, calculation only select the areas where right across the Gobi-Altai fault along 276, 4, and 233 Tracks because the far field regions including atmospheric and topographic noises. Elastic upper layers with 30 km misfit value are omitted on Figure 18 because the misfit value are quite similar to the upper layer 20 km. Figure 19 shows the best fitting seismogenic thickness 10 km, the same result can be found in Figure 19b Track 4 and Figure 18c Track 233, which tracks reflect most of tectonic signal. As for Track T276 (Figure 19a) and Track T462 (Figure 19d), the minimum misfits are not in agreement with the central two tracks. The reason why the variation between different tracks

is that the Track 276 and T462 InSAR rate map are not very robust to reflect surface deformation.

When searching the range of viscosities for the lower layer, in the low viscosity scenarios, the misfit curve has a much steeper gradient than is the case at high viscosities, which suggests that the lower bound of viscosity is stronger. From Figure 18, the minimum misfit value corresponds to viscosities is close from 5×10^{19} to 5×10^{21} Pa s. However, considering the late stage postseismic deformation rate has low signal-to-noise ratio, the misfit curve is flat at higher viscosity, and so the lower bound is a viscosity of 9×10^{19} Pa s. Therefore, the optimal model consists of an upper layer with thickness 10 km, and a half space with a viscosity of > 9×10^{19} Pa s. Detailed discussion of previous studies of viscosity under Gobi-Altai fault are present in Chapter 5.4.

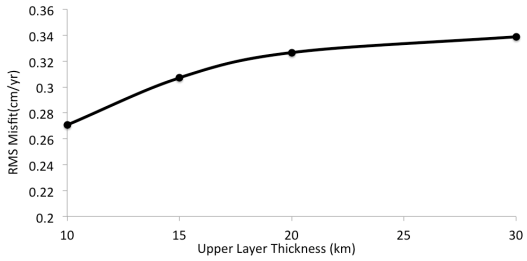

Figure 17. Result of Maxwell viscoelastic modeling. Misfit against upper layer thickness (from 10, 15, 20, 30 km).

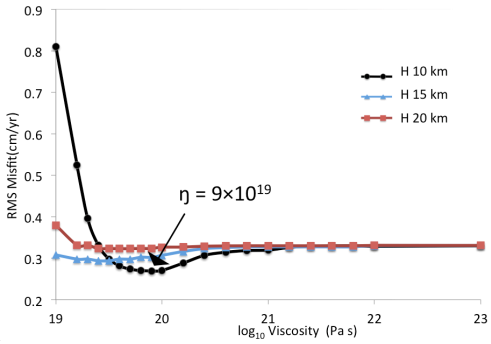

Figure 18. Overall RMS result of Maxwell viscoelastic modeling. RMS misfit against underlying substance (from 1×10^{19} Pa s to 1×10^{23} Pa s). The black, blue, and red line refers to the 10 km, 15 km, 20 km seismogenic thickness respectively.

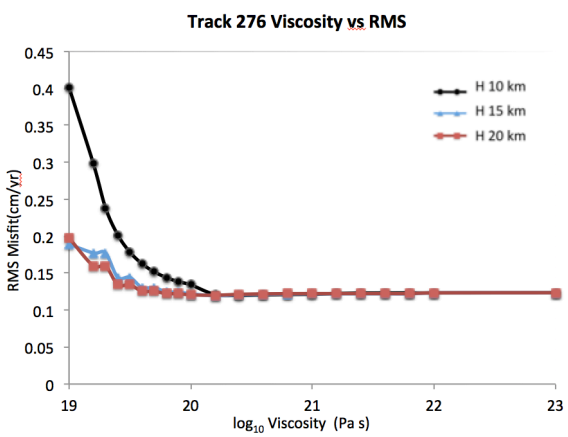

(a)

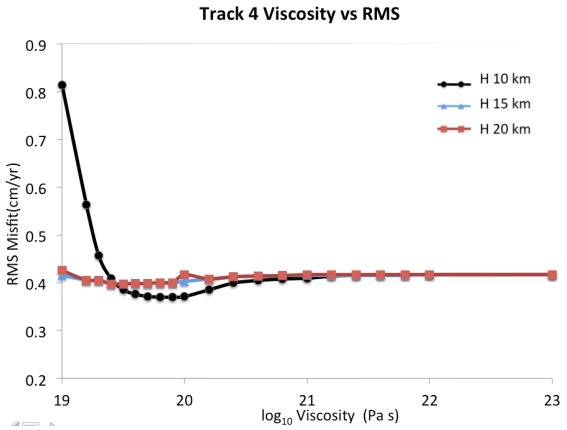

(b)

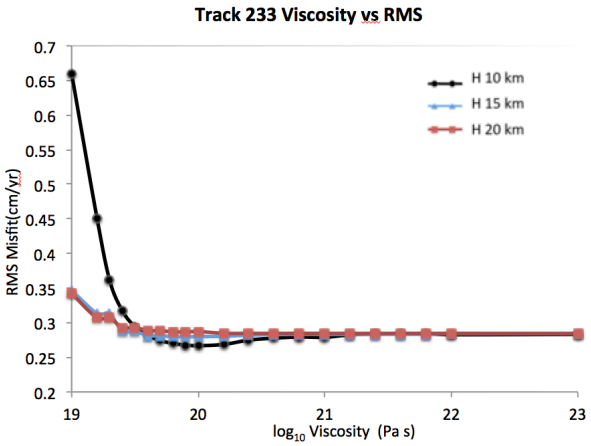

(c)

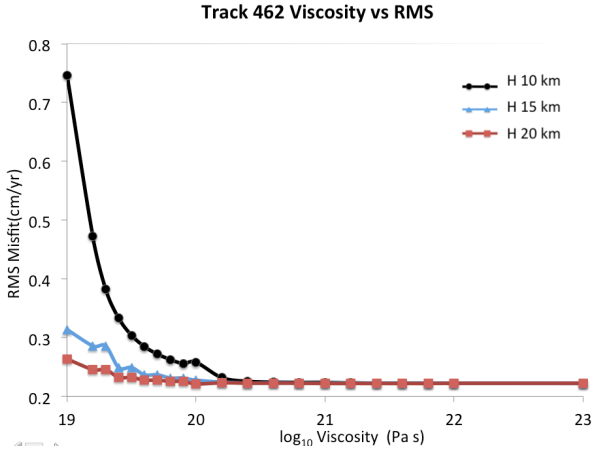

(d)

Figure 19, Root-mean-square misfit on Tracks 276, 4, 233 and 462 separately. RMS misfit against underlying substance (from 1×10^{19} Pa s to 1×10^{23} Pa s). The black, blue, and red line refers to the 10 km, 15 km, 20 km seismogenic thickness respectively.

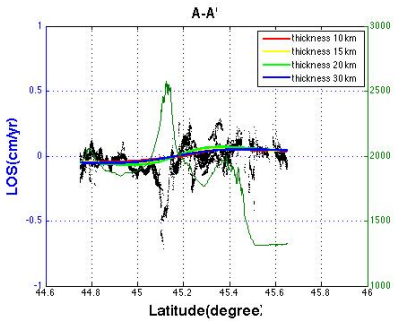
A-A'
thickness 10 km
thickness 15 km
thickness 20 km
thickness 30 km
LOS(cm/yr)
Latitude(degree)

(a)

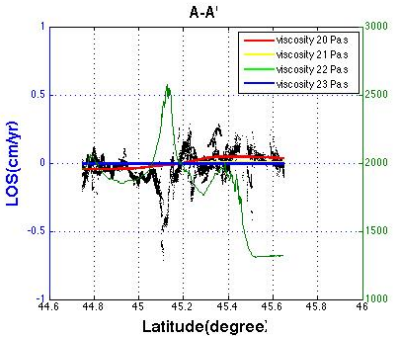
A-A'
viscosity 20 Pa.s
viscosity 21 Pa.s
viscosity 22 Pa.s
viscosity 23 Pa.s
LOS(cm/yr)
Latitude(degree)

(a')

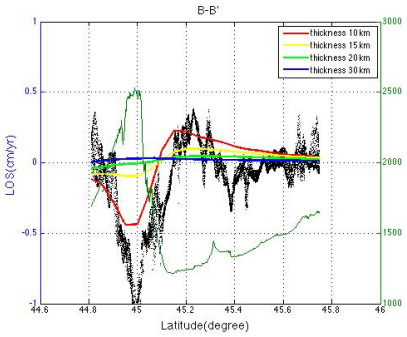
B-B'
thickness 10 km
thickness 15 km
thickness 20 km
thickness 30 km
LOS(cm/yr)
Latitude(degree)

(b)

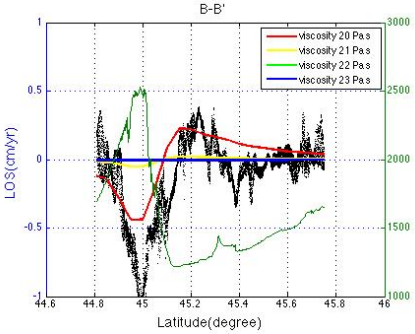
B-B'
viscosity 20 Pa.s
viscosity 21 Pa.s
viscosity 22 Pa.s
viscosity 23 Pa.s
LOS(cm/yr)
Latitude(degree)

(b')

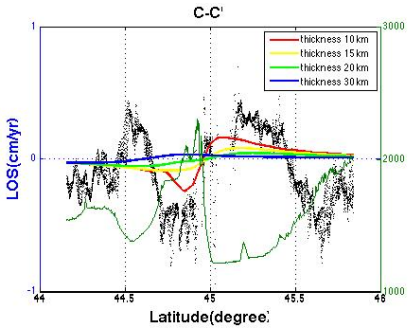
C-C'
thickness 10 km
thickness 15 km
thickness 20 km
thickness 30 km
LOS(cm/yr)
Latitude(degree)

(c)

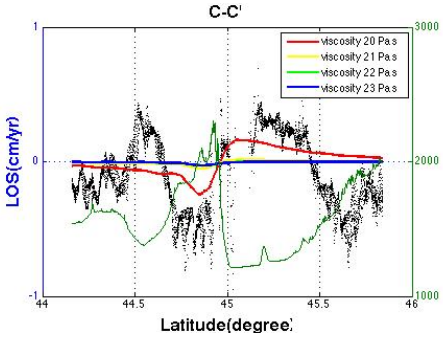
C-C'
viscosity 20 Pa.s
viscosity 21 Pa.s
viscosity 22 Pa.s
viscosity 23 Pa.s
LOS(cm/yr)
Latitude(degree)

(c')

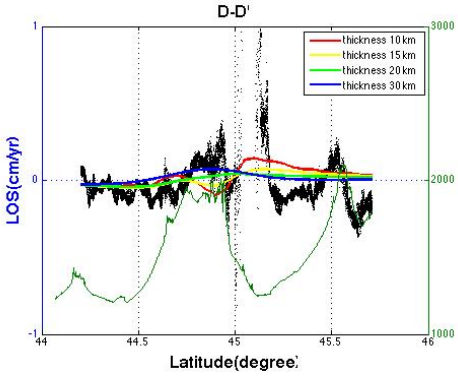
D-D'
thickness 10 km
thickness 15 km
thickness 20 km
thickness 30 km
LOS(cm/yr)
Latitude(degree)

(d)

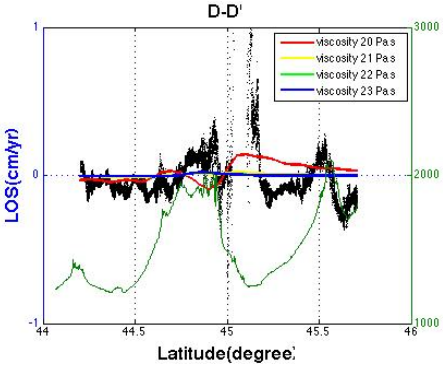
D-D'
viscosity 20 Pa.s
viscosity 21 Pa.s
viscosity 22 Pa.s
viscosity 23 Pa.s
LOS(cm/yr)
Latitude(degree)

(d')

Figure 20. Velocity profile plots across the main strike slip fault along A-A', B-B', C-C', D-D' (lines shown in Fig. 3). The black dots show the line-of-sight displacement rates (cm/yr) from the InSAR data, and the colored lines show the different models corresponding to increasing upper layer thickness (10 km, 15 km, 20 km, 30 km) and viscosity (1×10^{20} Pa s, 1×10^{21} Pa s, 1×10^{22} Pa s, 1×10^{23} Pa s) respectively. The best fitting viscoelastic relaxation model is for H = 10 km with 1×10^{20} Pa s viscosity, always shown by the red line of the model profiles. The second y-axis at the right side shows the elevation (m), the dark blue line in the profile displays the elevation plot.

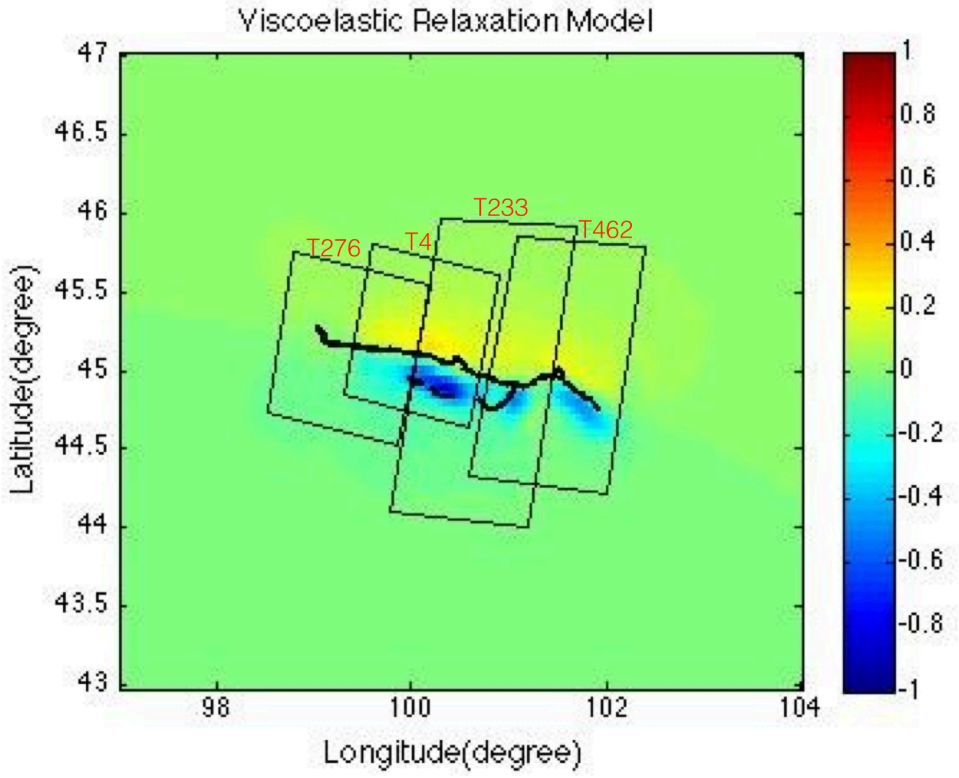

Figure 21. Optimal viscoelastic relaxation model (with upper layer thickness 10 km, viscosity 9×10^{19} Pa s) for the Gobi-Altai fault. Velocity components predicted from VISCO1D viscoelastic relaxation model. Thick black line marks the fault trace. T276, T4, T233 and T462 refer to SAR tracks 276, 4, 233 and 462, marked by thin black line boxes. Colour scale shows line-of-sight deformation rate in cm/yr.

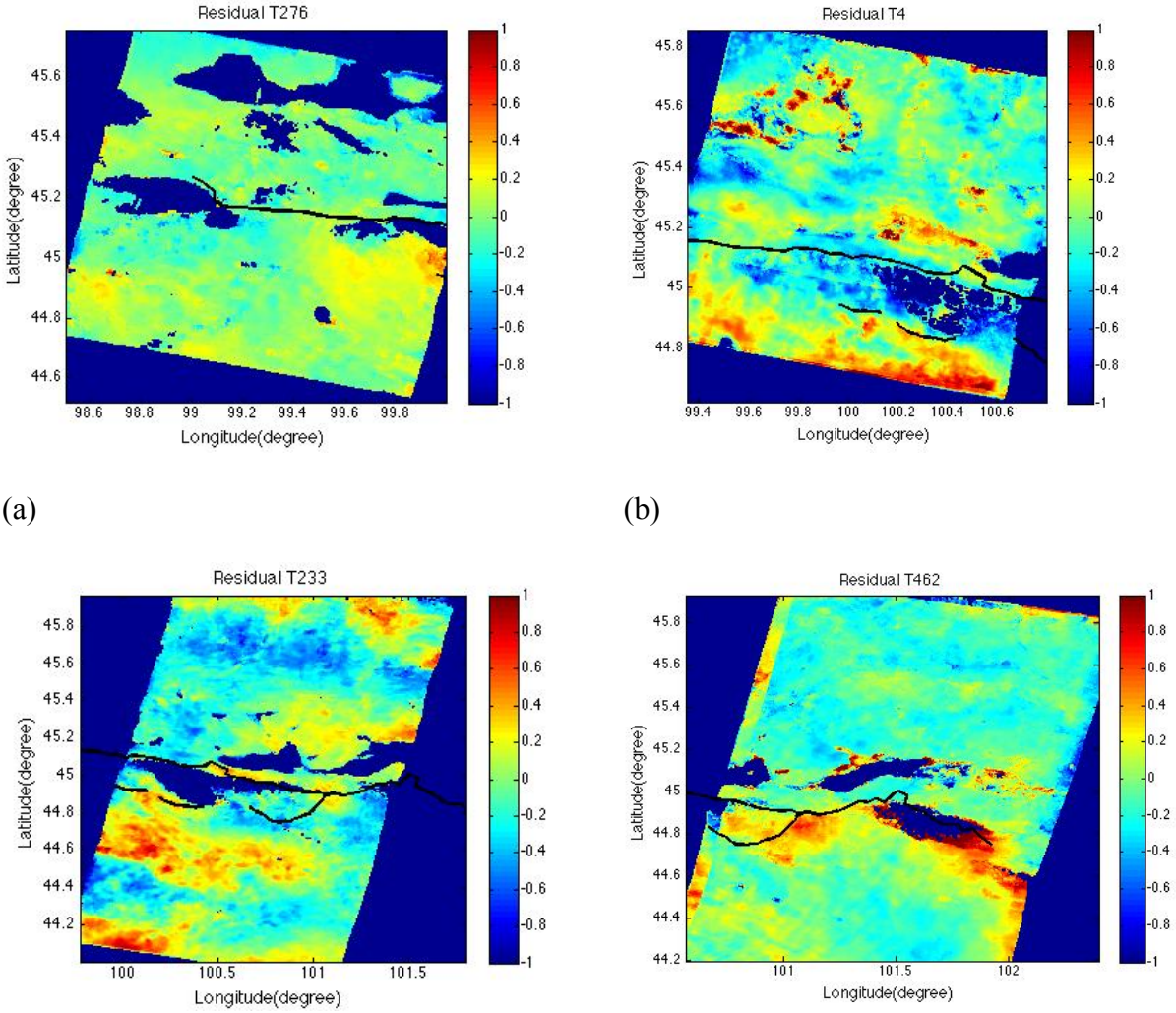

Figure 22. Viscoelastic relaxation models are shown in different tracks from west to east along the main Gobi-Altai fault: Track 276 (a), Track 4 (b), Track 233 (c), Track 462 (d). Black line marks fault trace. Colour scale shows deformation rate in cm/yr.

There are two explanations may explain the big residual on Figure 22d. Track 462. Firstly, the InSAR observation mainly contains topographic noise, which shows in Figure 20d, 20d'. The black surface deformation is consistent with the elevation change in dark green line. Secondly, at the end of the whole Gobi-Altai fault, the Kurushin et al. (1997) fault parameters at this region are not including a thrust component locates south of the fault. The detailed

discussion is in Chapter 5.1.

To summarise the viscoelastic relaxation modelling results, it is concluded that, under the hypothesis of a Maxwell rheology: (1) relaxation occurred in the lower crust; (2) the viscosity of the lower crust is $> 9\times10^{19}$ Pa s. The Maxwell relaxation time corresponding to this viscosity is 95.13 years.

4.2 Afterslip model

4.2.1 Method

Afterslip is an aseismic creep process that takes place on the fault following an earthquake. The slip rate usually decays to zero over time. Afterslip lasting from days to decades often has been detected (e.g., Savage et al. 2005). For example, after the Mw 9.2 Alaska earthquake, Suito and Freymueller (2009) observed afterslip continuing for longer than 40 years following the earthquake, with a rate of ~1 cm/yr during that period.

From the observed postseismic signal for strike-slip faults, similar surface deformation is expected for afterslip and viscoelastic relaxation, which makes it difficult to distinguish viscoelastic relaxation from afterslip (Ryder et al., 2007, 2011; Wen et al., 2012). It is reasonable to postulate that afterslip on the fault and its extension at depth can explain the postseismic surface motion. In general, afterslip occurs deeper than the coseismic slip. For example, see Owen et al. (2002) for the Hector Mine event, and Fialko (2004) for the Landers event, and Hsu et al. (2002) for the Chi-Chi event. Considering the postseismic afterslip may occur at any depth, it cannot be used to constrain the afterslip locking depth. Some

postseismic afterslip studies have simply chosen a subjective maximum depth. This question was addressed in this study by running the inversion for a range of upper and lower locking depths. The upper depth ranges lay between 0.25 to 14 km, and the lower locking depth between 5 and 80 km. The 2D search uses a uniform afterslip rate of 1.2 mm/yr (Calais et al., 2003), based on the formulation of Okada (1985). The aim is to determine whether afterslip can explain the InSAR-derived surface displacement rate map. In order to identify a minimum value of root-mean-square misfit, a number of models have been established for calculating the amount of misfit. The overall afterslip modelling misfit is computed for different upper and lower locking depths (Figure 23).

4.2.2 disloc3d

The Matlab code disloc3d.m computes surface and internal movements due to inclined shear and tensile faults in a half-space. The detailed mathematical development is derived from elastic dislocation theory, which is presented in Okada (1985) and Okada (1992). Okada (1985) lists equations to compute the surface displacements, strains, and stresses due to slip on a rectangular fault in an elastic half-space. Okada (1992) expands the expressions to calculate the internal deformation. Previously, the fortran code dc3d.f was written by Okada in 1991, and Peter Cervelli later converted the code to run in Matlab. To reproduce the displacements, input parameters used are: (1) the shear modulus 3×10^{10} Pa; (2) the Lamé parameter 3×10^{10} Pa; (3) 18 segments with fault parameters listed in Table 2 (entitled Summary of Displacements Along the 1957 Surface Rupture, from Kurushin et al. (1997)); (4) observation points in UTM projection.

A 2D misfit calculation is performed with upper locking depths ranging from 0.25 km to 14 km and lower locking depths from 5 km to 80 km. As can be seen on the afterslip misfit plot (Figure 23), the optimal afterslip model suggests that the afterslip happened both on the rupture plane and its extension (Vergnolla et al., 2003; Kenner and Segall, 2000). The curst thickness in this region is about 42 km- 57 km (Stachnik et al., 2014). However, the misfit value of different models just change slightly, which indicates afterslip occurring in the lower crust and down to the mantle. A forward model afterslip displacement is shown in Figure 23 with an upper locking depth 0.25 km, and a lower depth of 40 km, though, this may not be the best solution.

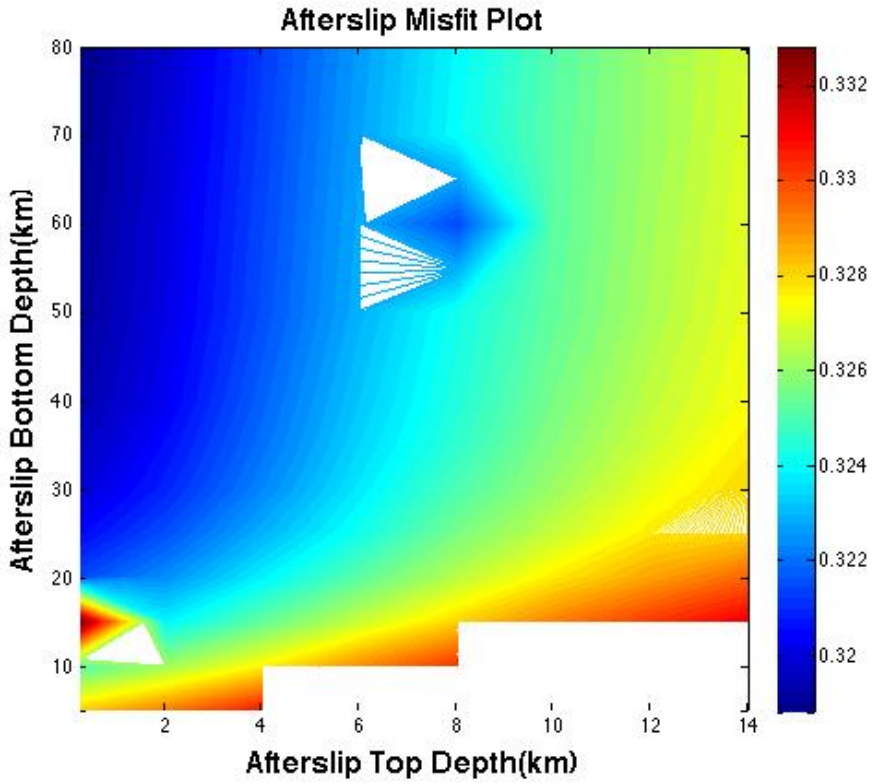

Figure 23. Contour plots of afterslip inversion top depth against bottom depth, the slip rate fixed as 1.2 mm/yr (Calais et al., 2003), colour scale refers to RMS misfit.

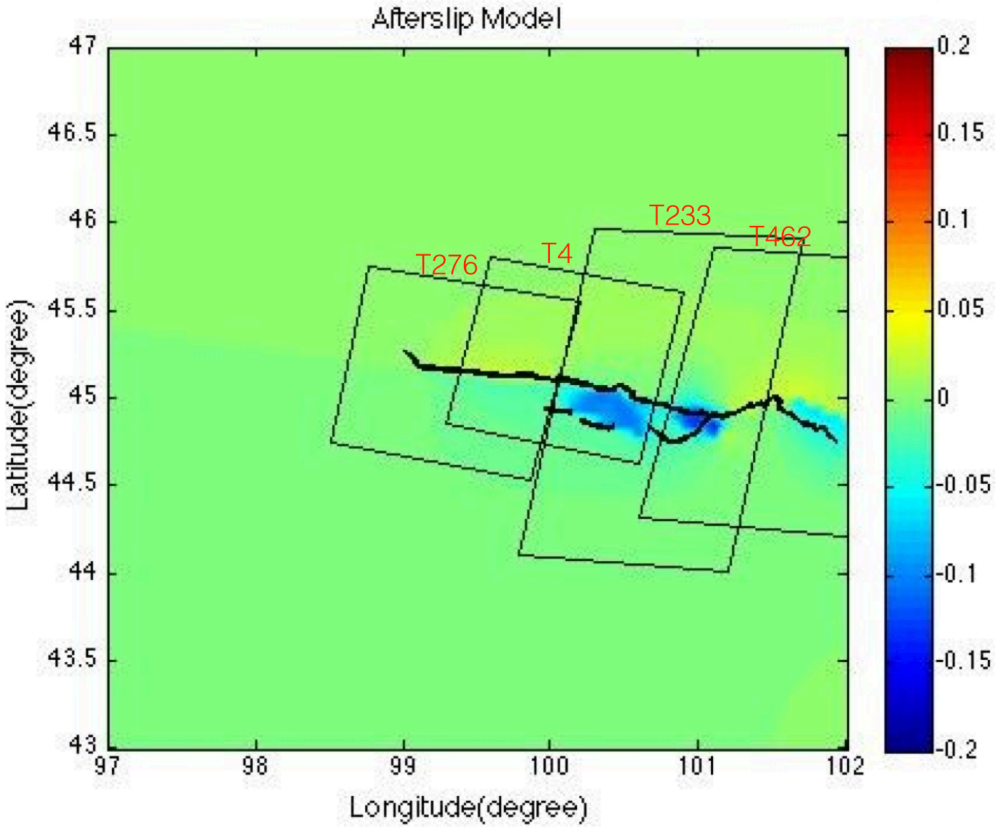

Figure 24. Afterslip inversion (with top depth as 0.25 km, bottom depth as 40 km) for the Gobi-Altai fault. Slip rate fixed as 1.2 mm/yr (Calais et al., 2003). Fault parameters for 18 segments derive from Kurushin et al. (1997) However, the RMS misfit plot (Figure 23) is not robust. And this model might not be the best solution.

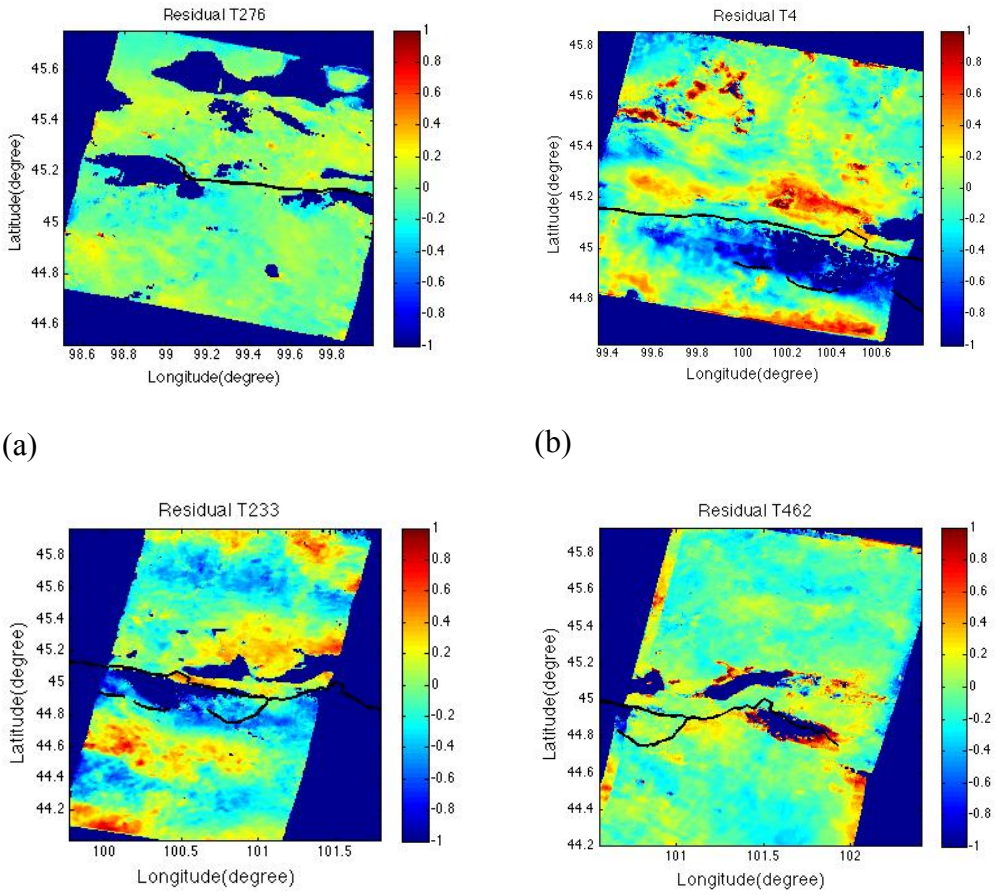

Figure 25. Afterslip model residuals are shown different tracks from west to east along the main Gobi-Altai fault: Track 276 (a), Track 4 (b), Track 233 (c), Track 462 (d). Black line marks fault trace. Colour scale shows line-of-sight deformation rate in cm/yr.

The comparisons are made between best fitting viscoelastic relaxation and afterslip model. The RMS value is comparing the models with InSAR rate map. On Track 276, the viscoelastic relaxation residual RMS misfit is 0.1384 cm/yr, whereas the afterslip RMS misfit value is 0.1215 cm/yr. On Track 4, the viscoelastic relaxation residual RMS misfit is 0.3702 cm/yr, and afterslip RMS misfit value is 0.4085 cm/yr. The misfit on Track 233, viscoelastic relaxation and afterslip misfit are 0.2678 cm/yr and 0.2799 cm/yr respectively. On final Track 462, viscoelastic relaxation and afterslip misfit are 0.2678 cm/yr and 0.2799 cm/yr respectively. The central two Tracks 4 and 233 reflect the most tectonic signal, and

viscoelastic relaxation RMS misfit on these two tracks is smaller than the afterslip misfit respectively. InSAR observation on Track 276 does not show significant relative movements due to the small number of SAR acquisitions. And Track 462 rate map contains an amount of topographic noise. The afterslip model misfit is smaller than the viscoelastic relaxation model on Tracks 276 and 462. Considering the validity of the misfit value, the conclusion can be made that the InSAR data is successfully explained by postseismic viscoelastic stress relaxation.

4.3 Interseismic Model

4.3.1 Method

Interseismic slip occurs on zone beneath the fault plane. Under the condition of strike-slip movement, the fault is locked from the surface to a shallow depth but slips by a constant rate below that depth (Savage and Burford, 1970). For the interseismic strain, it is equal to the coseismic strain magnitude accumulated in a longer time scale but opposite in sign (Segall et al., 2000). After an entire earthquake cycle, the strain in the blocks either side of the fault is zero. It is crucial to remember that the interseismic deformation is derived from the dislocation line rather than at the displacement surface. In this study, the routines of Okada (1992) were used to model interseismic deformation for constant slip on a rectangular fault plane. The free parameter in this model is the upper depth for the fault. The model searches for the minimum misfit by varying the upper depth between 3 km – 15 km, with the lower depth fixed at 35 km (Calais et al., 2003). The interseismic slip rate is 1 mm/yr in the Gobi-Altai region, which is estimated from GPS measurement based on stress accumulation (Calais et al., 2003). This uniform interseismic slip rate was used for all 18 segments of detailed fault

parameters from Table 2 (Kurushin et al., 1997) in an interseismic model based on Okada (1992). Figure 26 represents an interseismic deformation model with upper locking depth 15 km. In Figure 26, the interseismic deformation shows the negative lobe at the south side of the fault, which can be thought as a left-lateral mechanism. However, the positive signal on north of the fault is disappearing. The observed surface deformation may not derive from interseismic movement. The magnitude of the interseismic rate is smaller than the InSAR rate map, with a range from -0.2~0.2 cm/yr (from forward model).

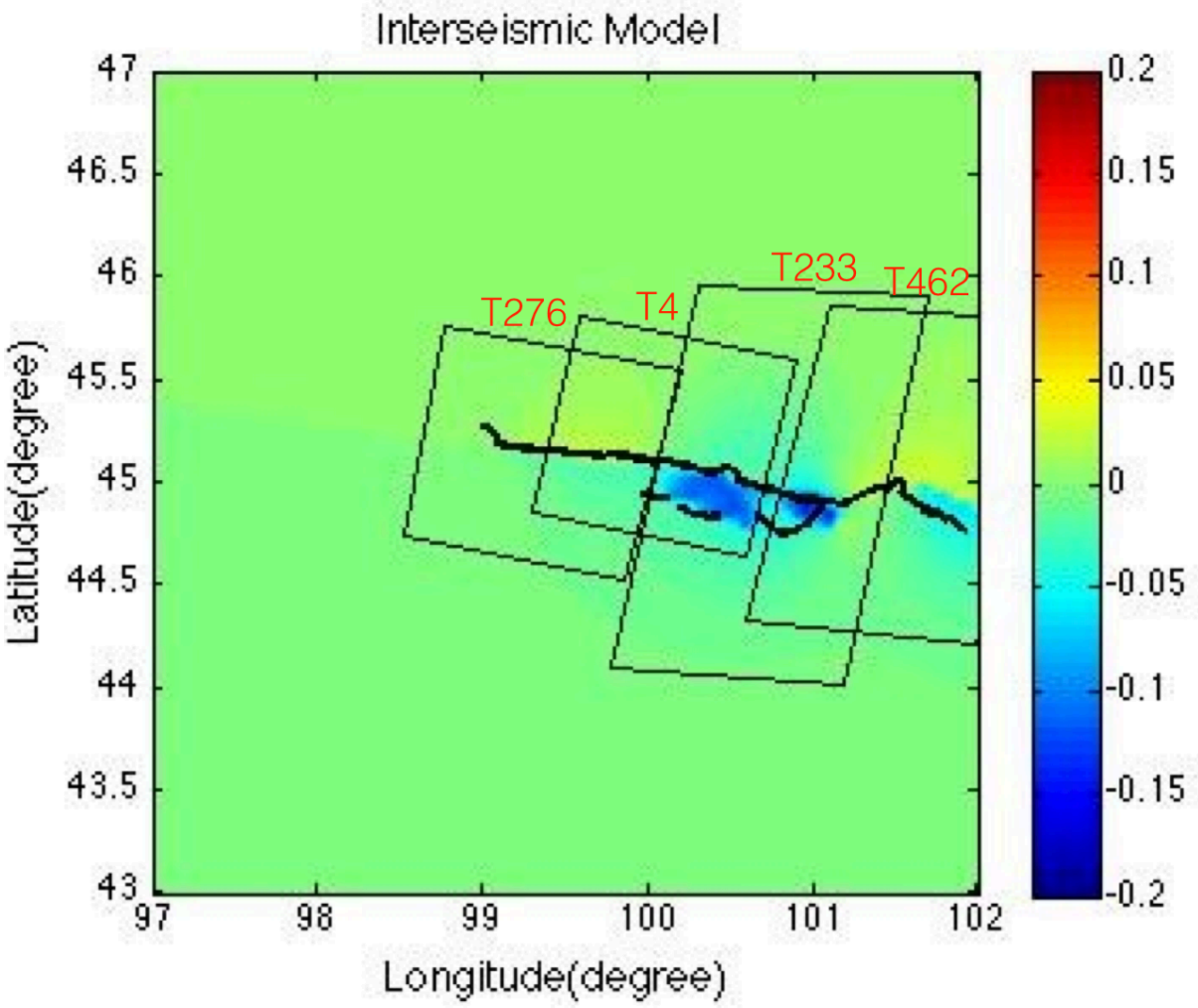

Figure 26. Interseismic slip model for the Gobi-Altai fault (top depth 0.25 km, lower depth 35 km). Black line marks the fault trace. Colour scale shows deformation rate in cm/yr.

Chapter 5

Discussion

5.1 Seismogenic thickness and effective elastic thickness in Gobi-Altai region

Wright et al., (2013) conclude that there is no clear relationship between seismogenic thickness and elastic thicknesses, for seismically active regions globally. Generally, the elastic thicknesses from Bouguer gravity are systematically larger than the geodetic seismogenic thicknesses (Wight et al., 2013). The geodetic observations may be relevant to weaker areas, and localized mechanisms can also modify the local rheology. From thermobarometric and petrologic analysis of mantle and lower crustal xenoliths, the crust-mantle boundary beneath the Gobi-Altai region in southwest Mongolia is located at a depth of 45 km (Ionov et al., 1998).

Both the effective elastic thickness and seismogenic thickness reflect the lithosphere strength of the upper crust. The effective strength of the continental lithosphere is in the seismogenic crust. This study using InSAR rate map and viscoelastic modelling constrain the seismogenic thickness of Gobi-Altai. Most of continental earthquakes occurred in the lower crust at depths less than 20 km, which can be defined as seismogenic crust (Wright et al., 2013). Bayasgalan et al. (2005) determine 10 earthquake centroid depths by investigating P and SH waveforms, and claim that the seismogenic thickness (Ts) within Mongolia is less than 20 km. This conclusion is consistent with this study. Through searching for best fitting viscoelastic relaxation models at various elastic upper layer thicknesses (Figure 18), the minimum misfit

model was that the seismogenic thickness is 10 km in Gobi-Altai region. Bayasgalan et al. (2005) also constrain the effective elastic thickness (Te) in central Mongolia is < 10 km, and infer the Gobi-Altai range may be a little greater but less than 20 km. Using free-air gravity profile across the Valley of Lakes in the Gobi-Altai to find the minimum misfit in the Gobi-Altai region, the result shows the effective elastic thickness is 10 km. In the Hangay dome and surrounding aseismic area, earthquakes centroid depths are less than 20 km. The spectral analysis of admittance presents an average effective elastic thickness of < 10 km over the broad region (Bayasgalan et al., 2005). The solid gravity analysis confirms that Te is comparable to Ts in Gobi-Altai region. This conclusion is in agreement with Maggi et al. (2000a).

5.2 Viscosity

A number of postseismic studies identify some general patterns for lower crust or upper mantle rheology. Wight et al., (2013) found 49 studies which postseismic observations have been made on continental earthquakes, and conclude the range of Maxwell viscosities across all studies between 1×10^{17} and 7×10^{19} Pa s. For the standard linear solid and Burgers viscoelastic modeling, the range is 1×10^{17} to 2×10^{20} Pa s (Wright et al., 2013).

The late-stage postseismic investigation of the Gobi-Altai region suggests a range of viscosities from 1×10^{16} to 1×10^{19} Pa s (Barbot et al., 2008; Pollitz, 2003; Vergnolle et al., 2003). Vergnolle et al. (2003), using GPS measurements, found an upper mantle viscosity between 1×10^{18} and 4×10^{18} Pa s. When they test various mantle viscosities beneath Mongolia, they found that both a high viscosity model ($5\times10^{20}< \eta_m< 1\times10^{21}$ Pa s) (η_m refers to the viscosity in the mantle) and a low-viscosity model ($1\times10^{18}<\eta_m < 4\times10^{18}$ Pa s) fit the GPS data. Their statistical tests slightly favor the low-viscosity model in their study, and the low

viscosity value is in agreement with this study 9×10^{19} Pa s. This viscosity is also consistent with other strike-slip fault studies in Tibet Plateau. For example, Ryder et al. (2014) find the lower crust has viscosity 6-10×10^{19} Pa s under the Beng Co strike-slip fault. Wen et al. (2012) exploit the best fitting viscosity for the mid-to-lower crust of 2-5×10^{19} Pa s along the western part of the Kunlun fault. Barbot et al. (2008) constrain a lower bound viscosity on Altai fault of 10^{19} Pa s. Calais et al. (2002) use GPS method to study the readjustment after M_w 8.4 1905 Bolnay earthquake, and assumed a lower crust viscosity of 3×10^{18} Pa s. Gourmelen and Amelung (2005) using a two-layer model find a lower bound of the underlying substrate of 1-10 $\times10^{18}$ Pa s on Central Nevada Seismic Belt. The viscosity values of these studies give confidence to the conclusion that the viscosity under Gobi-Altai fault is $< 9\times10^{19}$ Pa s.

On the contrary, regional studies (Stosch et al., 1995; Kopylova et al., 1995; Ionov et al., 1998; Déverchère et al., 2001) indicate that the lower crust may be composed of diabase, and extrapolation of the geotherm of Ionov et al. (1998) combined with application of flow laws for wet diopside or dry diabase (Mackwell et al., 1998) supports the model of a relatively strong lower crust.

5.3 Analysis of viscoelastic relaxation, afterslip, and interseismic models

Postseismic motion associated with large strike-slip fault may be the result of viscoelastic relaxation, afterslip or a mixture of these two end-member models (Wright et al., 2013; Wen et al., 2012). The different mechanisms at depth also display very similar displacement fields at the surface (e.g., Hearn, 2003). How to distinguish between afterslip and viscoelastic relaxation is a major challenge for InSAR studies. The observed and modeled line-of-sight InSAR rate maps are shown in Figures 6 and 20 respectively. From a comparison of the

viscoelastic relaxation and afterslip models with the InSAR dataset along four tracks, both the viscoelastic relaxation model and afterslip model show the similar pattern of line-of-sight surface displacement. For special fault and satellite geometries, the afterslip and viscoelastic relaxation can be separated from each other. For example, after the 1999 Hector Mine earthquake, the most important cause of surface displacement is inferred to be viscoelastic relaxation (Pollitz et al., 2001). For the present study, even if the published GPS data (Calais et al., 2003) cover the Gobi-Altai fault, the GPS stations located on both sides of Gobi-Altai fault are sparse. Therefore, it is impossible to identify the actual mechanism responsible for the deformation along the Gobi-Altai fault. In addition, the complex surface ruptures in this region consist of left-lateral strike-slip movement and several thrust faults, which make the interpretation of InSAR velocity map difficult. The observed surface dislocation may be a mixture of left-lateral motion and thrust related uplift.

Afterslip is assumed to occur from the top of the crust right down to the mantle in some cases (Biggs et al., 2009; Ryder et al., 2007,2011). The afterslip misfit plot (Figure 23) prefer to a deep afterslip situation. This result is in contrast to the afterslip earthquakes studied by InSAR method globally, in which the lower depth of faulting is shallow for most of the strike-slip ruptures (most of depth around 10-15 km, but no more than 24 km) (Wright et al., 2013). The optimal afterslip model in Figure 24 shows the afterslip with top depth 0.25 km, lower depth of 40 km is fit for the InSAR observation. But this deep afterslip may in fact be a viscoelastic relaxation (Wight et al., 2013).

Furthermore, in consideration of the long period after the main shock, and the deformation signal having low signal-to-noise ratio, it is informative to run models of interseismic displacement for the Gobi-Altai Fault. The interseismic slip distribution from the model

inversion is shown in Figure 26. The parameter 35 km depth of seismogenic thickness are acquired from Calais et al. (2003), which infer the Bogd strike-slip faults locked from the surface and down to the lower crust. Through the interseismic model shows a negative signal at the south side of the Gobi-Altai fault, which may reflects a known left-lateral movement. But the broad positive colour on the north side of the fault is disappearing, which is not in agreement with the observed surface displacement. It is concluded that the observed postseismic deformation is not primarily interseismic creep on a localized shear zone.

From the perspective of timescale, investigations of afterslip motions usually measure a decay on timescales of months to years (Savage et al., 2005). However, a recent InSAR postseismic deformation study in Tabas (Copley, 2014) observes continuing afterslip lasting up to 30 years after the Mw 7.3 1978 Tabas-e-Golshan thrust-faulting earthquake in eastern Iran. Another example of long-term afterslip is the Mw 9.2 1964 Alaska earthquake. This afterslip continued for more than 40 years following the earthquake, with the slip rate was 1 cm/yr during the InSAR observation period. Johnson et al. (2009) investigated the afterslip beneath the rupture patch following the 2002 Mw 7.9 Denali earthquake and found that it declined to zero within 4.5 years of the event. For the Loma Prieta earthquake (Segall et al., 2000) case, the afterslip decayed to near zero within 5 years. And most of studies suggest the afterslip is a shorter-lived process (e.g. Bürgmann et al., 2002; Freed, 2007; Hsu et al., 2002). Ryder et al. (2014) claim that the observed should be solely contribute to the viscoelastic relaxation across Beng Co fault because the SAR data covers fifth and sixth postseismic decades. In this study, the InSAR rate map (from 1995 to 2010) rule out the afterslip still occurs on Gobi-Altai fault due to the time scale and deep afterslip situation.

Vergnolle et al. (2003) determined the shear zone velocity associated with the low-viscosity

model (3 to 5.5 mm/yr), and it is more consistent with the accumulated slip rate on active faults in Mongolia (Ritz et al., 1995, 2003). The amplitude of the line of sight velocities measured right across the Gobi-Altai fault is ~6 mm/yr, equivalent to a left-lateral rate of 15.35 mm/yr. This slip rate is larger than the results measured by dating offset alluvial fans along profiles at depth (Vassallo et al., 2005). Vassallo et al., (2005) measure the slip rates along the Bogd strike-slip fault over the Upper Pleistocene-Holocene is 0.95±0.29 mm/yr. Rizza et al. (2011) based on dating ^{10}Be data measuring the left-lateral slip rate is ~1mm/yr. Calais et al. (2002) using GPS data from 1997 to 2000 period measure the surface velocities can be 4 mm/yr. Calais et al. (2002) also run the VISCO1D modelling and find the postseismic effects to the GPS velocities presented is less than 2 mm/yr for Mongolian sites, and on the Baikal sites are less than 1 mm/yr. Calais et al. (2002) detect that the Bolnay postseismic postseismic deformation may still contribute up to 7 mm/yr in western Mongolia. Considering the large slip rate differences between this study and previous investigations, the conclusion can be made that the observed InSAR surface deformation may reflect a late-stage postseismic deformation mainly contribute by viscoelastic relaxation. However, other studies may measure a steady interseismic deformation.

5.4 Strike-slip and thrust component

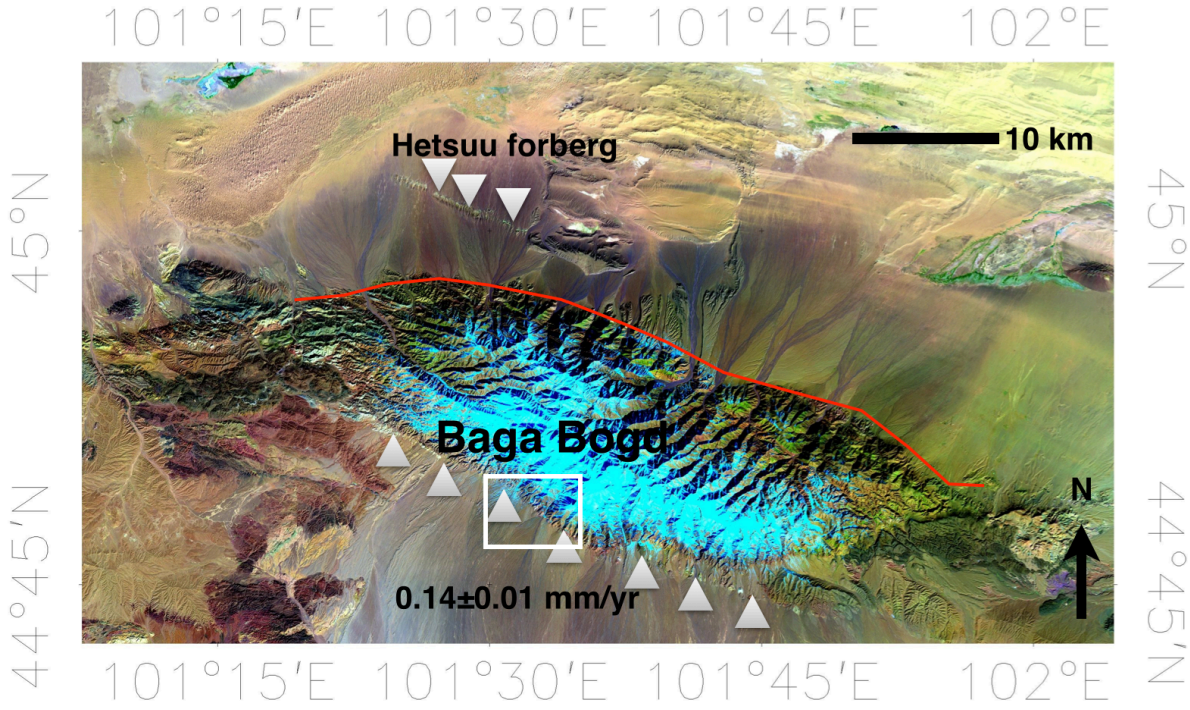

Figure 27. Landsat ETM +7 image shows left-lateral strike-slip and thrust component at the end segment of the main Gobi-Altai fault. White triangles are marked with the thrust segments ruptured before or after 1957 event. Red line indicates the left-lateral strike-slip with a slight reverse dip-slip faulting.

Large strike-slip faults are always accompanied by a thrust component at the end of the fault, e.g. the Kunlun and San Andreas faults (Bayarsayhan et al., 1996; Wen et al., 2012). Bayarsayhan et al. (1996) assert that the San Andreas fault and the thrust faults nearer Los Angeles will alter the hazard posed by ruptures on both the strike-slip and thrust components. The 1971 San Fernando earthquake occurred on the main thrust fault dipping towards the San Gabriel Mountains (Heaton, 1982). Wen et al. (2012) find the largest aftershock for November 14th 2001 Mw 7.8 Kokoxili earthquake is mostly a thrust event. For the Gobi-

Altai case, the reverse rupture on the Gurvan Bulag or Bayan Tsagaan nuruu thrust faults may have affected the stress accumulation in this area (Kurushin et al., 1997). The analysis from Pollitz (2003) suggests that the 1957 Gobi-Altai earthquake triggered by the rupture of a thrust segment. They take the Bayan Tsagaan nuruu thrust fault as an example, using the first motion solution of Okal (1976) to estimate the reverse dip-slip faulting on an east-west striking, 45° dipping secondary fault. This hypothesis is consistent with that proposed by Kurushin et al. (199) that the Gobi-Altai left-lateral rupture may have initiated with rupture of the Tsagaaan nuruu thrust fault at the western of the Bogd fault and then propagated to the east as a left-lateral strike-slip fault. It is possible that thrust and strike-slip components of slip are spatially separated onto individual surface structures that meet at depth.

Chapter 6

Conclusion

6.1 Postseismic study

InSAR rate maps of southwest Mongolia have been used to observe the postseismic deformation in the Gobi-Altai region 38-53 years after the main shock. An obvious red to blue transition zone is displayed on the rate map (Figure 6), which shows a known left-lateral strike-slip mechanism. After searching for the various seismogentic thickness under the viscoelastic relaxation condition, the best fitting model support the seismogenic thickness as 10 km. Comparing the seismogenic thickness (10 km) with the effective elastic thickness (10 km) obtained from Bayasgalan et al. (2005), the lithospheric thickness in the Gobi-Altai region is consistent with the perspective of seismic and gravity.

Using a simple two-layer model with Maxwell body rheology, under a lower bound on the upper layer thickness of the crust of 10 km circumstance, a viscosity of the lower crust and upper mantle of 9×10^{19} Pa s was found. The Maxwell relaxation time corresponding to this viscosity is 95.13 years. The viscoelastic relaxation happened in the lower crust and upper mantle.

After comparing the viscoelastic relaxation, afterslip, and interseismic models by searching the minimum misfit value, the InSAR observed postseismic deformation mainly record the viscoelastic relaxation. Assuming the observed deformation represents long-lasting afterslip, the afterslip is located in the lower crust and upper mantle. But the deep afterslip shown in a few cases indicates the deep afterslip may actually reflect viscoelastic relaxation.

The final part of Gobi-Altai fault is not well studied. The InSAR velocity map contains highly topographic noise on Track 462 (Figure 6d). All of analysis is established on review other papers. Gobi-Altai left-lateral rupture have initiated with rupture of the Tsagaaan nuruu thrust fault at the western of the Bogd fault and then propagated to the east as a left-lateral strike-slip fault. How the thrust segments at the south end of the Gobi-Altai fault interact with the strike-slip segments in depth still an open question.

6.2 Avenues for progress

The InSAR rate map is affected by atmospheric noise, part of which is likely to be strongly correlated with topography. This problem could be resolved by using π-RATE software. The π-Rate stacking approach is derived from the multi-interferogram method developed by Biggs et al. (2007), Elliott et al. (2008) and Wang et al. (2012) have developed the method into Matlab-based software. This technique uses network corrections to correct orbital error, and also estimate a DEM-correlated atmospheric error and atmospheric phase screen and it has proved to be successful in several fault-related studies (Wang et al., 2009; Wang and Wright, 2012; Garthwaite et al., 2013; Ryder et al., 2014). Dr. Hua Wang assists me to re-process the Gobi-Altai InSAR rate map using π-RATE software. The re-processed velocity maps in this study are shown in Appendix B.

There also exists the possibility of another approach to decrease the atmospheric noise based on individual MODIS datasets. This software has been written by David Bekaert (Ph.D. candidate, University of Leeds). The use of these methods to decrease noise in the InSAR rate map would increase the confidence of the signal. Due to the small magnitude of tectonic signal, atmospheric and topographic noise remove is important. If the InSAR noise reduction

is successful, the data may warrant modeling using a three-layer viscoelastic structure beneath the study region. A disadvantage of the two-layer modeling carried out in this study is that it precludes analysis the structure of lower crust and upper mantle. In the present study it is not possible to discriminate between strong crust, weak mantle or the combination of strong crust, strong mantle beneath the Gobi-Altai region. It would be useful to develop three-layer models, although this will require greater computing power and longer model run times.

When interferograms measure the deformation of the Earth's surface, only one component of the satellite's line of sight direction is measured (Fialko et al., 2004). If GPS data are available in this region, future work may involve combining InSAR results with independent GPS datasets in order to analyse the horizontal and vertical movements in the study area.

References

Aki K., and Richards, P., 1980, Quantitative seismology: Theory and methods: San Francisco, W. H. Freeman and Company, 932 p.

Avouac, J. P., and P. Tapponnier (1993), Kinematic model of active deformation in central Asia, Geophys. Res. Lett., 20, 895– 898.

Baljinnyam, I., and 10 others, 1993, Ruptures of major earthquakes and active deformation in Mongolia and its surroundings: Geological Society of America Memoir 181, 62 p.

Barbot, S., Y. Hamiel, and Y. Fialko (2008), Space geodetic investigation of the coseismic and postseismic deformation due to the 2003 Mw7.2 Altai earthquake: Implications for the local lithospheric rheology, J. Geophys. Res., 113, B03403, doi:10.1029/2007JB005063.

Barruol, G, Deschamps, A, Deverchere, J, Mordvinova, V, Ulziibat, M, Perrot, J, Artemiev, A, Dugarmaa, T, & Bokelmann, G 2008, 'Upper mantle flow beneath and around the Hangay Dome, central Mongolia', Earth And Planetary Science Letters, 274, 1-2, pp. 221-233, GeoRef, EBSCOhost.

Bayasgalan, A. & Jackson, J., 1999. A re-assessment of the faulting in the 1967 Mogod earthquakes in Mongolia, Geophys. J. Int., 138, 784–800.

Bayasgalan, A., Jackson, J., Ritz, J.-F. & Carretier, S., 1999a. Field examples of strike-slip fault terminations in Mongolia, and their tectonic significance, Tectonics, 18, 394–411.

Bayasgalan, A., Jackson, J., McKenzie, D. (2005) Lithosphere rheology and active tectonics in Mongolia: relations between earthquake source parameters, gravity and GPS measurements. Geophysical Journal International 163 (3), 1151-1179

Bayarsayhan, C., A. Bayasgalan, B. Enhtuvshin, Kenneth W. Hudnut, R. A. Kurushin, Peter Molnar, and M. Ölziybat(1996), 1957 Gobi-Altay, Mongolia, earthquake as a prototype for southern California's most devastating earthquake Geology, July, 1996, v. 24, p. 579-582, doi:10.1130/0091-7613

Biggs, J., Wright, T., Lu, Z.&Parsons, P., 2007. Multi-interferogram method for measuring inter seismic deformation: Denali Fault, Alaska, Geophys. J. Int., 170, 1165–1179.

Biggs, J., et al. (2009), The postseismic response to the 2002 M 7.9 Denali Fault earthquake: Constraints from InSAR 2003–2005, Geophys. J. Int.,176, 353–367, doi:10.1111/j.1365-246X.2008.03932.x.

Bürgmann, R., et al. (2002), Time-space variable afterslip on and deep below the Izmit earthquake rupture, Bull. Seismol. Soc. Am., 92, 126–137, doi:10.1785/0120000833.

Bürgmann, R., and G. Dresen (2008), Rheology of the lower crust and upper mantle: Evidence from rock mechanics, geodesy and field observations, *Ann. Rev. Earth Plan. Sci.*, 36, doi:10.1146/annurev.earth.36.031207.124326, 531-567.

Bürgmann, R., and Thatcher, W., 2013, Space geodesy: A revolution in crustal deformation measurements of tectonic processes, in Bickford, M.E., ed., The Web of Geological Sciences: Advances, Impacts, and Interactions: Geological Society of America Special Paper 500, p. 397–430, doi:10.1130/2013.2500(12).

Burov, E. and Watts, A. (2006). The long-term strength of continental lithosphere: jelly sandwich or cr`eme brˆul´ee? GSA Today, 16, 1:4–10.

Burgers, J.M., 1939. Mechanical considerations—model systems— phenomenological theories of relaxation and of viscosity, in First Report on Viscosity and Plasticity, pp. 5–72, prepared by the committee for the study of viscosity of the Academy of Sciences at Amsterdam, Nordmann Publishing Company, Inc., New York.

Calais, E., M. Vergnolle, J. Deverchre, V. Sankov, A. Lukhnev, andS. Amarjargal, Are postseismic effect of the M = 8.4 Bolnay earthquake (July 12, 1905) still influencing GPS velocities in the Mongolia-Baikal area?, Geophys. J. Int., 148, 1 –12, 2002

Calais, E., M. Vergnolle, V. San'kov, A. Lukhnev, A. Miroshnitchenko, S. Amarjargal, and J. De´verche`re, GPS measurements of crustal deformation in the Baikal-Mongolia area (1994–

2002): Implications for current kinematics of Asia,J. Geophys. Res., 108(B10), 2501, doi:10.1029/2002JB002373, 2003.

Cavalié, O., M.-P. Doin, C. Lasserre, and P. Briole (2007), Ground motion measurement in the Lake Mead area, Nevada,by differential synthetic aperture radar interferometry time series analysis: Probing the lithosphere rheological structure, J. Geophys. Res., 112, B03403, doi:10.1029/2006JB004344.

Chen, W.P., and Molnar, P., 1977, Seismic moments of major earthquakes and the average rate of slip in Central Asia: Journal of Geophysical Research, v. 82, p. 2945–2969.

Chen, Q., Freymueller, J.T., Yang, Z., et al., 2004. Spatially variable extension in southern Tibet based on GPS measurements. Journal of Geophysical Research 109, B09401. http://dx.doi.org/10.1029/2002JB002350.

Copley A., Postseismic afterslip 30 years after the 1978 Tabas-e-Golshan (Iran) earthquake: observations and implications for the geological evolution of thrust belts, Geophys. J. Int. first published online February 20, 2014 doi:10.1093/gji/ggu023

Cunningham 1996 :Late Cenozoic transpression in southwestern Mongolia and the Gobi-Altai-Tien Shan connection

Cunningham,W.D., 1998. Lithospheric controls on late Cenozoic construction of the Mongolian Altai, Tectonics, 17, 891–902.

Cunningham, D., 2005. Active intracontinantal tranpressional mountain building in the Mongolian Altai: defining a new class of orogen, Earth. planet. Sci. Lett., 240, 436–444.

Clark, M. K., and Royden, L. H., 2000, Topographic ooze: Building the eastern margin of Tibet by lower crustal flow, Geology, 28, 703–706.

Déverchère, J., C. Petit, N. Gileva, N. Radziminovitch, V. Melnikova, and V. San'kov, Depth distribution of earthquakes in the Baikal rift and its implications for the rheology of the lithosphere, Geophys. J. Int., 146,714–730, 2001.

Doin, M.P., Lasserre, C., Peltzer, G., Cavaliè, O. & Doubre, C., 2009. Correc- tions of stratified tropospheric delays in SAR interferometry: validation with global atmospheric models, J. appl. Geophys., 69(1), 35–50.

England, P. & McKenzie, D. 1982. A thin viscous sheet model for continental deformation. Geophysical Journal of the Royal Astronomical Society, 70,295–321.

England, P.C., McKenzie, D.P. (1983), Correction to: A thin viscous sheet model for continental deformation. Geophys. JlR. astr. Soc. 73, 523-532.

England, P. & Houseman, G. 1985. Role of lithospheric strength heterogeneities in the tectonics of Tibet and neighbouring regions. Nature, 315, 297–301,doi:10.1038/315297a0.

England, P. & Houseman, G. 1986. Finite strain calculations of continental deformation. Comparison with the India-Asia collision zone. Journal of Geophysical Research, 91, 3664–3676, doi:10.1029/JB091iB03p03664.

England, P. C., and P. Molnar (1997b), Active deformation of Asia: From kinematics to dynamics, Science, 278, 647– 650.

Elliott, J.R., Biggs, J., Parsons, P. & Wright, T.J., 2008. InSAR slip rate determination on the Altyn Tagh Fault, northern Tibet, in the presence of topographically correlated atmospheric delays, Geophys. Res. Lett.,35(12), doi:10.1029/2008GL033659.

Elliott, J.R., Walters, R.J., England, P.C., Jackson, J.A., Li, Z., Parsons, B., 2010b. Extension on the Tibetan plateau: recent normal faulting measured by InSAR and body wave seismology. Geophysics Journal International 183, 503–535. http://dx.doi.org/10.1111/j.1365-246X.2010.04754.x.

England P., P. Molnar (2005). Late Quaternary to decadal velocity fields in Asia. J. Geophys. Res., 110, B12401, doi:10.1029/2004JB003541.

Farr, T.G.&Kobrick, M., 2000. Shuttle Radar Topography Mission produces a wealth of data, EOS, Trans. Am. geophys. Un., 81, 583–585.

Federal Aviation Administration

http://www.faa.gov/about/office_org/headquarters_offices/ato/service_units/techops/navservices/gnss/gps/

Fialko Yuri. Evidence of fluid-filled upper crust from observations of post-seismic deformation due to the 1992 Mw7.3 Landers earthquake. J. Geophys. Res., 109 , B08401, doi:10.1029/2004JB002985, 2004

Flügge, W., 1967. Viscoelasticity, 119p., Blaisdell Publishing Company, Waltham, Massachusetts.

Freed, A.M., Bürgmann, R., Calais, E., Freymueller, J.T., and Hreinsdóttir, S., 2006b, Implications of deformation following the 2002 Denali, Alaska, earthquake for postseismic relaxation processes and lithospheric rheology: Journal of Geophysical Research, v. 111, B01401, doi:10.1029/2005JB003894.

Freed, A. M., and R. Bürgmann (2004), Evidence of power-law flow in the Mojave desert mantle, Nature, 430, 548–551, doi:10.1038/nature02784.

Freed, A., et al. (2006a), Implications of deformation following the 2002 Denali, Alaska, earthquake for postseismic relaxation processes and lithospheric rheology, J. Geophys. Res., 111, B01401, doi:10.1029/2005JB003894.

Freed, A. M.(2007), Afterslip (and only afterslip) following the 2004 Parkfield, California, earthquake, Geophys. Res. Lett., 34, L06312,doi:10.1029/2006GL029155.

Flesch, L. M., W. E. Holt, and A. J. Haines (2001), Dynamics of the India- Eurasia collision zone, J. Geophys. Res., 106, 16,435–16,460.

Flugge, W.1975. Viscoelasticity, 2nd ed. New York: Springer-Verlag

Florensov, N. A., and Solonenko, V. P., editors,1963, The Gobi-Altai earthquake: Moscow,Akademiya Nauk USSR, (in Russian; English translation, 1965, U.S. Department of Commerce, Washington, D.C.), 424 p.

Fialko, Y. (2004), Evidence of fluid-filled upper crust from observations of postseismic deformation due to the 1992 Mw7.3 Landers earthquake, J. Geophys. Res., 109, B08401, doi:10.1029/2004JB002985.

Garthwaite, M.C., Wang, H. & Wright, T.J., 2013. Broadscale interseismic deformation and fault slip rates in the central Tibetan Plateau observed using InSAR, J. geophys. Res., 118(9), 5071–5083.

Garcia-Sancho, Tesauro and Govers, in prep. 2014. A consistent geodynamic model for predicting the velocity and plate-internal deformation of Eurasia, Wegener conference abstract

Ghiglia, D. C. and Pritt, M. D. (1998), Two-dimensional phase unwrapping: theory, algorithms, and software, John Wiley & Sons, Inc, New York.

Goldstein, R.M., Zebker, H.A.&Werner, C.L., 1988. Satellite radar interferometry: Two-dimensional phase unwrapping, Radio Sci., 23(4), 713–720.

Gourmelen, N. & Amelung, F., 2005. Postseismic mantle relaxation in the central Nevada seismic belt, Science, 310(5753), 1473–1476.

Gray, A.L., Mattar, K.E. & Sofko, G., 2000. Influence of ionospheric elec- tron density fluctuations on satellite radar interferometry, Geophys. Res.Lett., 27(10), 1451–1454.

Gross, S., and C. Kisslinger (1997), Estimating tectonic stress rate and state with Landers aftershocks, J. Geophys. Res., 102(B4), 7603–7612, doi:10.1029/96JB03741.

Gross, S., and R. Bürgmann (1998), Rate and state of background stress estimated from the aftershocks of the 1989 Loma Prieta, California, earthquake, J. Geophys. Res., 103(B3), 4915–4927, doi:10.1029/97JB03010.

Hanssen, R.F., 2001. Radar Interferometry: Data Interpretation and Error Analysis, Kluwer.

Heaton, T., 1982, The 1971 San Fernando earthquake:A double event? Seismological Society of America Bulletin, v. 72, p. 2037–2062.

Hazarika, D., Kumar, N., Yadav, D., (2013) Crustal thickness and Poisson's ratio variations across the northwest Himalaya and eastern Ladakh, Acta Geophysica doi:10.2478/s11600-013-0128-y

Hearn, E.H., Bürgmann, R., and Reilinger, R., 2002, Dynamics of Izmit earthquake postseismic deformation and loading of the Duzce earthquake hypocenter: Bulletin of the Seismological Society of America, v. 92, p. 172–193, doi:10.1785/0120000832.

Hearn, E. H. (2003), What can GPS data tell us about the dynamics of postseismic deformation?, Geophys. J. Int., 155, 753–777, doi:10.1111/j.1365-246X.2003.02030.x.

Hearn, E. H., et al. (2009), Izmit earthquake postseismic deformation and dynamics of the North Anatolian Fault Zone, J. Geophys. Res., 114, B08405, doi:10.1029/2008JB006026.

Hetland, E., Hager, B., 2006. The effects of rheological layering on post-seismic deformation. Geophysical Journal International 166, 277–292.

Houseman, G. & England, P. 1986. Finite strain calculations of continental deformation. I - Method and general results for convergent zones II - Comparison with the India-Asia collision zone. Journal of Geophysical Research, 91, 3651–3663, doi:10.1029/JB091iB03p03651.

Hsu, Y., N. Bechor, P. Segall, S. Yu, L. Kuo, and K. Ma (2002), Rapid afterslip following the 1999 Chi-Chi, Taiwan Earthquake, Geophys. Res. Lett., 29(16), 1754, doi:10.1029/2002GL014967.

Ionov, D., S. Y. O'Reilly, and W. L. Griffin, A geotherm and lithospheric section for central Mongolia (Tariat region), in Mantle Dynamics and Plate Interactions in East Asia, Geodyn. Ser., vol. 27, edited by M. J. F.

Flower et al., pp.127–153, AGU, Washington, D. C., 1998. Jackson, J. A. & White, N. J., 1989. Normal faulting in the upper continental crust: observations from regions of active extension. Journal of Structural Geology, 11, 15--36.

Johnson, K.M., Hilley, G.E., Bürgmann, R., 2007. Influence of lithosphere viscosity structure on estimates of fault slip rate in the Mojave region of the San Andreas fault system. Journal of Geophysical Research 112, B07408. http://dx.doi.org/10.1029/2006JB004842.

Johnson, K. M., R. Bürgmann, and J. Freymuller (2009), Coupling afterslip and viscoelastic flow following the 2002 Denali Fault, Alaska earthquake, Geophys. J. Int., 176, 670–682, doi:10.1111/j.1365-246X.2008.04029.x.

Jolivet, Jean-Francois Ritz, Riccardo Vassallo, Christophe Larroque, Regis Braucher, Munkhjargal Todbileg, Alain Chauvet, Christian Sue, Nicolas Arnaud, Raquel de Vicente, Anastasia Arzhanikova and Serguei ArzhanikovMongolian summits; an u plifted, flat, old but still preserved erosion surface,Geology (Boulder)(October 2007), 35(10):871-874

Stachnik, J.; Anne Meltzer; Stephanie Souza; Ray Russo, (2014), Crustal and upper mantle structure of the Hangay Dome, central Mongolia, http://www.iris.edu/hq/meetings/2014/06/iris_workshop_sunriver_oregon/scihi/WebPages/0111.html

Kelin Wang, Yan Hu& Jiangheng He, Deformation cycles of subduction earthquakes in a viscoelastic Earth, Nature 484, 327–332 (19 April 2012) doi:10.1038/nature11032

Kenner, S. J., and P. Segall, Postseismic derformation following the 1906 San Francisco earthquake, J. Geophys. Res., 105, 13,195– 13,209, 2000.

Kurushin, R.A., Bayasgalan, A., Ölziybat, M., Enkhtuvshin, B.,Molnar, P., Bayarsayhan, C., Hudnut, K.W., Lin, J., 1997. The surface rupture of the 1957 Gobi-Altay, Mongolia, earthquake. Geol. Soc. Am. Spec. Pap. 320.

Khil'ko, S.D., R.A. Kurushin, V.M. Kochetkov,I. Balzhinnyam, and D. Monkoo, Strong earthquakes, paleoseismogeological and nacroseismic data, in Earthquakes and the Bases .l'br Seismic Zoning of Mongolia, Transactions 41, The Joint Soviet-Mongolian Scientific Geological Research Expedition,: pp. 19-83, Nauka, Moscow,1985. Liu, H., Geodynamic

Kopylova, M. G., S. Y. O'Reilly, and Y. S. Genshaft, Thermal state of the lithosphere beneath Central Mongolia: Evidence from deep-seated xenoliths from the Shavaryn-Saram volcanic centre in the Tariat depression, Hangai, Mongolia, Lithos, 36, 243–255, 1995.

Lacassin, R., Valli, F., Arnaud, N. et al. 2004b. Reply to Comment on 'Largescale geometry, offset and kinematic evolution of the Karakoram fault,Tibet'. Earth and Planetary Science Letters, 229, 159–163.

Leloup, P.H. & Kienast, J.-R. 1993. High-temperature metamorphism in a major strike-slip shear zone: the Ailao Shan–Red River, People's Republic of China. Earth and Planetary Science Letters, 118, 213–234.

Maggi, A., Jackson, J.A., McKenzie, D. & Priestley, K., 2000a. Earthquake focal depths, effective elastic thickness, and the strength of the continental lithosphere, Geology, 28, 495-498.

Marone, C. J., C. H. Scholz, and R. Bilham (1991), On the mechanics of earthquake afterslip, J. Geophys. Res., 96, 8441–8452. Massonnet, D., Feigl, K., Rossi, M. & Adragna, F., 1994. Radar interferometric mapping of deformation in the year after the Landers earthquake.Nature, 369, 227–230.

Massonnet, D., Feigl, K., 1998. Radar interferometry and its application to changes in the earth's surface. Reviews of Geophysics 36 (4), 441-500.

Mackwell, S. J., M. E. Zimmerman, and D. L. Kohlstedt, High-temperature deformation of dry diabase with application to tectonics on Venus, J. Geophys. Res., 103, 975– 984, 1998.

McClusky, S. (2000). Global positioning system constraints on plate kinematics and dynamics in the eastern Mediterranean and Caucasus. J. Geophys. Res., 105:5695–5719.

Molnar, P., Fitch, T. J., and Wu, F. T. (1973). Fault plane solutions of shallow earthquakes and contemporary tectonics in Asia. Earth Planet. Sci. Lett., 19:101–112.

Molnar, P. and Tapponnier, P. (1975). Cenozoic Tectonics of Asia: Effects of a continental collision. Science,189(4201):419–426.

Molnar, P., and P. Tapponnier (1978), Active tectonics of Tibet, J. Geophys. Res., 83(B11), 5361–5375, doi:10.1029/JB083iB11p05361.

Molnar, P. & Deng, Q., 1984. Faulting associated with large earthquakes and the average rate of deformation in central and eastern Asia, J. geophys.Res., 89, 6203–6227.

Nur, A., and Mavko, G., 1974, Postseismic viscoelastic rebound: Science, v. 183, p. 204–206, doi: 10.1126/science.183.4121.204.

Nyst,M.&Thatcher,W., 2004. New constraints on the active tectonic deformation of the Aegean, J. geophys. Res., 109, doi:10.1029/2003JB002830.

NASA Landsat Program, 2000, Landsat ETM+ scene L720001020_z47 USGS, 10/20/2000.

Okal, E.A., 1976. A surface-wave investigation of the rupture mechanism of the Gobi-Altai (December 4, 1957) earthquake, Phys. Earth planet. Inter., 12, 319-328.

Okada, Y. (1985), Internal deformation due to shear and tensile faults in a half space, Bull. Seismol. Soc. Am., 82, 1018–1040.

Okada, Y. (1992), Internal deformation due to shear and tensile faults in a half-space, Bulletin of the Seismological Society of America April 1992 82:1018-1040

Ozawa, T., and H. Ueda (2011), Advanced interferometric synthetic aperture radar (InSAR) time series analysis using interferograms of multiple-orbit tracks: A case study on Miyake-jima, J. Geophys. Res., 116, B12407, doi:10.1029/2011JB008489.

Owens, T.J., Zandt, G., 1997. Implications of crustal property variations for models of Tibetan plateau evolution. Nature 387, 37–43.

Owen, S., G. Anderson, D.C. Agnew, H. Johnson, K. Hurst, R. Reilinger,Z.-K. Shen, J. Svarc, and T. Baker (2002), Early postseismic deformation from the 16 October 1999 Mw 7.1 Hector Mine, California, earthquake as measured by survey-mode GPS, Bull. Seismol. Soc. Am., 92, 1423–1432.

Pacheco, J.F. & Sykes, L.R., 1992. Seismic moment catalog of large shallow earthquakes, 1900 to 1989, Bull. Seismol. Soc. Am., 82, 1306–1349.

Pollitz. F, Postseismic relaxation theory on a layered spherical Earth, J. geophys. Res., 102 , 17921(1992).

Pollitz, F., G. Peltzer, and R. Bürgmann (2000), Mobility of continental mantle: Evidence from postseismic geodetic observations following the 1992 Landers earthquake, J. Geophys. Res., 105, 8035–8054, doi:10.1029/1999JB900380.

Pollitz, F. F. (2001), Viscoelastic shear zone model of a strike-slip earthquake cycle, J. Geophys. Res., 106(B11), 26541–26560, doi:10.1029/2001JB000342.

Pollitz, F., 2003. Transient rheology of the uppermost mantle beneath the Mojave Desert, California. Earth and Planetary Science Letters 215, 89–104.

Peltzer, G., et al. (1998), Poroelastic rebound along the Landers 1992 earthquake surface rupture, J. Geophys. Res., 103, 30,131–30,145, doi:10.1029/98JB02302.

Peltzer,G ., P. Rosen,F . Rogez, and K. Hudnut, Postseismirc rebound in fault step-overs caused by pore fluid flow, Science,2 73, 1202-1204,1996b.

Peltzer, G., and P. Tapponnier (1988), Formation and evolution of strike slip faults, rifts, and basins during the India-Asia collision: An experimental approach, J. G

Price, E. J., and R. Bu¨rgmann (2002), Interactions between the Landers and Hector Mine earthquakes from space geodesy, boundary element modeling, and time-dependent friction, Bull. Seismol. Soc. Am., 92, 1450 – 1469.

Rolland, Y., Maheo, G., Pêcher, A. & Villa, I. 2008. Syn-kinematic emplacement of the Pangong metamorphic and magmatic complex along the Karakoram Fault (north Ladakh). Journal of Asian Earth Sciences, doi:10.1016/j.aeaes.2008.03.009.

Rolland, Y. and Pêcher, A. 2001. The Pangong granulites of the Karakoram Fault (Western Tibet): vertical extrusion within a lithospheric scale fault? Comptes Rendus de

l'Acade´mie des Sciences, 332, 363–370.

Rosen, P.A., Hensley, S. & Peltzer, G., 2004. Updated Repeat Orbit Interferometry Package Released, EOS, Trans. Am. geophys. Un., 85(5), 35.

Replumaz, A., and P. Tapponnier (2003), Reconstruction of the deformed collision zone between India and Asia by backward motion of lithospheric blocks, J. Geophys. Res., 108(B6), 2285, doi:10.1029/2001JB000661.

Ritz, J. F., E. T. Brown, D. L. Bourle`s, H. Philip, A. Schlupp, G. M. Raisbeck, F. Yiou, and B. Enkhtuvshin, Slip rates along active faults estimated with cosmic-ray-exposure dates: Application to the Bogd fault, Gobi-Altay, Mongolia, Geology, 23, 1019– 1022, 1995.

Ritz, J.-F., et al., Late Pleistocene to Holocene slip rates for the Gurvan Bulag thrust fault (Gobi-Altay, Mongolia) estimated with ^{10}Be dates, J. Geophys. Res., 108(B3), 2162, doi:10.1029/2001JB000553, 2003.

Rigo, A., Chabalier, JB, Meyer.B , Armijo.R, The 1995 Kozani—Grevena (northern Greece) earthquake revisited: an improved faulting model from synthetic aperture radar interferometry, Geophysical Journal International 157 (2), 727-736

Rizza, M, Ritz, J, Braucher, R, Vassallo, R, Prentice, C, Mahan, S, McGill, S, Chauvet, A, Marco, S, Todbileg, M, Demberel, S, & Bourles, D 2011, 'Slip rate and slip magnitudes of past earthquakes along the Bogd left-lateral strike-slip fault (Mongolia)', Geophysical Journal International, 186, 3, pp. 897-927, GeoRef, EBSCOhost

Royden, L. H., B. C. Burchfiel, R. W. King, E. Wang, Z. Chen, F. Shen, and Y. Liu (1997), Surface deformation and lower crustal flow in eastern Tibet, Science, 276, 788–790.

Ryder, I., (2006) Elastic and Viscoelastic Modelling of Postseismic Motion and Fault Structures. Ph.D. thesis. Doctor of Philosophy, University of Oxford

Ryder, I., Parsons, B.E., Wright, T.J., and Funning, G.J., 2007, Postseismic motion following the 1997 Manyi (Tibet) earthquake: InSAR observations and modeling: Geophysical Journal

International, v. 169, doi: 10.1111/j.1365-1246X.2006.03312.x.

Ryder, I., Bürgmann, R., and Pollitz, F., 2011, Lower crustal relaxation beneath the Tibetan Plateau and Qaidam Basin following the 2001 Kokoxili earthquake: Geophysical Journal International, v. 187, doi: 10.1111/j.1365-1246X.2011.05179.x.

Ryder, I., H. Wang, L. Bie, A. Rietbrock (2014), Geodetic imaging of late postseismic lower crustal flow in Tibet, Earth Planet. Sci. Lett., 404: 136-143.

Rodriguez, E., Morris, C.S. & Belz, J.E., 2006. A Global Assessment of the SRTM Performance. J. Am. Soc. Photogrammetr. Remote Sens., 72(3),249–260.

Savage J. C. and Burford R. O. (1970). Accumulation of tectonic strain in California Bulletin of the Seismological Society of America, 60(6):1877-1896

Savage, J. C., and W. H. Prescott (1978). Asthenosphere readjustment and the earthquake cycle, J. Geophys. Res. 83, 3369–3376.

Savage, J. C. (1990), Equivalent strike-slip earthquake cycles in half-space and lithosphere-asthenosphere Earth models, J. Geophys. Res., 95,4873–4879, doi:10.1029/JB095iB04p04873.

Savage, J.C., Svarc, J.L. & Yu, S.-B., 2005. Postseismic relaxation and transient creep, J. geophys. Res., 110, doi:10.1029/2005JB003687.

Sandwell, D. T. and Price, E. J. (1998), Phase gradient approach to stacking interferograms, Journal of Geophysical Research, 103(B12):30183–30204.

Sandwell, D. T. and Sichoix, L. (2000), Topographic Phase Recovery from Stacked ERS Interferometry and a Low Resolution Digital Elevation Model, Journal of Geophysical Research, 105(B12): 28211–28222.

Schulmann, K., A. B. Thompson, O. Lexa, and J. Ježek, Strain distribution and fabric development modeled in active and ancient transpressive zones, J. Geophys. Res., 108(B1), 2023, doi:10.1029/2001JB000632, 2003.

Segall, P., Burgmann, R. & Matthews, M., 2000. Time-dependent triggered afterslip following the 1989 Loma Prieta earthquake, J. geophys. Res., 105, 5615–5634.

Sevkikavar, K.,Tatar, O., Piper, J., Kocbulut,F, Levent, Mesci, B,(2009) Determination of neotectonic features of the Karasu Basin (SE Turkey) and their relationship with Quaternary volcanic activity using Landsat ETM+ imagery, International Journal Of Remote Sensing, 30, 17, pp. 4507-4524, Environment Complete, EBSCOhost, viewed 7 August 2014.

Stosch, H. G., D. A. Ionov, I. S. Puchtel, S. J. G. Galer, and A. Sharpouri, Lower crustal xenoliths from Mongolia and their bearing on the nature of the deep crust beneath central Asia, Lithos, 36, 227– 242, 1995.

Suito, H. & Freymueller, J.T., 2009. A viscoelastic and afterslip postseismic deformation model for the 1964 Alaska earthquake, J. geophys. Res., 114, doi:10.1029/2008JB005954.

Shen, Z.-K., et al. (2003), Postseismic deformation modeling of the 2001 Kokoxili earthquake, western China, paper presented at EGS-AGUEUG Joint Assembly, Nice, France.

Tapponnier, P., G. Peltzer, A. Y. Le Dain, R. Armijo, and P. Cobbold (1982), Propagating extrusion tectonics in Asia: New insights from simple experiments with plasticine, Geology, 10, 611 –616.

Takeuchi, C., Fialko, Y., 2012. Dynamic models of interseismic deformation and stress transfer from plate motion to continental transform faults. Journal of Geophysical Research 117, B05403.

Tapponnier, P. & Molnar, P., 1979. Active faulting and Cenozoic tectonics of the Tien Shan, Mongolia, and Baykal regions, J. geophys. Res., 84, 3425–3459.

Thatcher, W., Matsuda, T., Kato, T., and Rundle, J.B., 1980, Lithospheric loading by the 1896 Riku-u earthquake, northern Japan: Implications for plate flexure and asthenospheric rheology: Journal of Geophysical Research, v. 85, p. 6429–6435,

doi: 10.1029/JB085iB11p06429.

Thatcher, W., and Rundle, J.B., 1984, A viscoelastic coupling model for the cyclic deformation due to periodically repeated earthquakes at subduction zones: Journal of Geophysical Research, v. 89, p. 7631–7640, doi: 10.1029/JB089iB09p07631.

Thatcher, W. (2003). GPS constraints on the kinematics of continental deformation. Int. Geol. Rev., 45:191–212.

Thatcher W. and Pollitz F., (2008), Temporal evolution of continental lithospheric strength in actively deforming regions.

Tiberi, C, Petit, C, Deschamps, A, Déverchère, J, Perrot, J, Appriou, D, Mordvinova, V, Artemiev, A, Dugaarma, T, & Ulzibaat, M 2008, 'Asthenospheric imprints on the lithosphere in Central Mongolia and Southern Siberia from a joint inversion of gravity and seismology (MOBAL experiment)', Geophysical Journal International, 175, 3, p. 1283-1297, Scopus®, EBSCOhost.

Vaghri, A., Hearn, E., 2012. Can lateral viscosity contrasts explain asymmetric interseismic deformation around strike-slip faults? Bulletin of the Seismological Society of America 102, 490–503.

Vassallo, R., Ritz, J.-F., Braucher, R. & Carretier, S., 2005. Dating faulted alluvial fans with cosmogenic 10Be in the Gurvan Bogd mountain range (Gobi-Altay, Mongolia): climatic and tectonic implications, Terra Nova, 17, 278–285.

Vassallo, R., et al. (2007), Transpressional tectonics and stream terraces of the Gobi-Altay, Mongolia,Tectonics, 26, TC5013, doi:10.1029/2006TC002081.

Valli, F., Arnaud, N., et al. 2007. Twenty million years of continuous deformation along the Karakorum fault, western Tibet: A thermochronological analysis. Tectonics, 26, TC4004, doi:10.1029/2005TC001913.

Valli, F., Leloup, P.H., et al. 2008. New U–Th/Pb constraints on timing of shearing and long-

term slip-rate on the Karakorum fault. Tectonics, 27, TC5007, doi:10.1029/2007TC002184.

Vergnolle, M., F. Pollitz, and E. Calais, Constraints on the viscosity of the continental crust and mantle from GPS measurements and postseismic deformation models in western Mongolia, J. Geophys. Res., 108(B10), 2502, doi:10.1029/2002JB002374, 2003.

Walker, R, Nissen, E, Molor, E, & Bayasgalan, A 2007, 'Reinterpretation of the active faulting in central Mongolia', Geology [Boulder], 35, 8, pp. 759-762, GeoRef, EBSCOhost, viewed 31 December 2014.

Wang, H., Wright, T.J. & Biggs, J., 2009. Interseismic slip rate of the northwestern Xianshuihe fault from InSAR data, Geophys. Res. Lett., 36(3), doi:10.1029/2008GL036560.

Wang, H., Wright, T.J., Yu, Y., Lin, H., Jiang, L., Li, C. & Qiu, G., 2012. InSAR reveals coastal subsidence in the Pearl River Delta, China, Geophys. J. Int., 191(3), 1119–1128.

Wen, Y., Li, Z., Xu, C., Ryder, I., Bürgmann, R., 2012. Postseismic motion after the 2001 MW7.8 Kokoxili earthquake in Tibet observed by InSAR time series. J.Geo-phys. Res.117 (B8).

Windley, B, & Allen, M 1993, 'Mongolian Plateau; evidence for a late Cenozoic mantle plume under Central Asia', Geology [Boulder], 21, 4, pp. 295-298, GeoRef, EBSCOhost.

Wright TJ; Elliott JR; Wang H; Ryder I (2013) Earthquake cycle deformation and the Moho: Implications for the rheology of continental lithosphere, Tectonophysics, 609, pp.504-523. doi: 10.1016/j.tecto.2013.07.029

Yamasaki, T., Wright, T., Houseman, G., 2013. Weak ductile shear zone beneath a major strike-slip fault: inferences from earthquake cycle model constrained by geodetic observations of the western North Anatolian Fault Zone. Journal of Geophysical Research.

Zebker, H.A., Rosen, P.A. &Hensley, S., 1997. Atmospheric effects in interferometric synthetic aperture radar surface deformation and topographic maps, J. geophys. Res., 102(B10), 7547–7563

Appendix A

Table A Interferogram list.

Scene 1 date (yymmdd)	Scene 2 date (yymmdd)	Direction	Satellite	Track	Perpendicular Baseline (m)	Duration (years)
010722	020811	Descending	ERS	276	-308	1.05
951231	960623	Descending	ERS	276	-244	0.48
951231	970330	Descending	ERS	276	114	1.25
960623	010722	Descending	ERS	276	114	5.08
960623	970330	Descending	ERS	276	358	0.77
960623	980104	Descending	ERS	276	121	1.53
970330	010722	Descending	ERS	276	-233	4.31
970330	980104	Descending	ERS	276	-237	0.76
980104	010722	Descending	ERS	276	44	3.55
980104	020811	Descending	ERS	276	-264	4.6
961022	970902	Descending	ERS	4	-233	0.86
970415	970520	Descending	ERS	4	-752	0.1
970415	970729	Descending	ERS	4	-625	0.29
970520	010109	Descending	ERS	4	-26	3.64
970520	970902	Descending	ERS	4	520	0.28
970520	980331	Descending	ERS	4	28	0.86
970520	980713	Descending	ERS	4	-59	1.15
970520	981201	Descending	ERS	4	-199	1.53
970729	970902	Descending	ERS	4	392	0.09
970729	971111	Descending	ERS	4	-293	0.28
970729	971216	Descending	ERS	4	-389	0.38
970729	980224	Descending	ERS	4	-460	0.57
970729	980331	Descending	ERS	4	-98	0.67
970729	980713	Descending	ERS	4	-187	0.96
970729	981201	Descending	ERS	4	-327	1.34
970902	971111	Descending	ERS	4	-686	0.19
970902	971216	Descending	ERS	4	-782	0.29
971111	971216	Descending	ERS	4	-96	0.1
971111	980224	Descending	ERS	4	-167	0.29
971111	980331	Descending	ERS	4	195	0.39
971111	980714	Descending	ERS	4	-340	0.67
971111	981201	Descending	ERS	4	-34	1.06
971216	010109	Descending	ERS	4	236	3.06
971216	980224	Descending	ERS	4	-70	0.19
971216	980331	Descending	ERS	4	291	0.29
971216	980713	Descending	ERS	4	203	0.58
971216	980714	Descending	ERS	4	-243	0.58

980224	980331	Descending	ERS	4	362	0.1
980224	980714	Descending	ERS	4	-172	0.39
980224	981201	Descending	ERS	4	133	0.77
980331	010109	Descending	ERS	4	-54	2.77
980331	980713	Descending	ERS	4	-88	0.28
980331	980714	Descending	ERS	4	-535	0.29
980331	981201	Descending	ERS	4	-228	0.67
980713	980714	Descending	ERS	4	-447	0.0037
980713	981201	Descending	ERS	4	-140	0.38
980714	981201	Descending	ERS	4	306	0.38
981201	010109	Descending	ERS	4	174	2.11
960620	970220	Descending	ERS	233	-191	0.67
960620	970501	Descending	ERS	233	-284	0.86
960620	970918	Descending	ERS	233	-405	1.24
960620	971127	Descending	ERS	233	430	1.44
960620	980101	Descending	ERS	233	201	1.53
960620	980312	Descending	ERS	233	-222	1.73
960620	980416	Descending	ERS	233	301	1.82
960620	980521	Descending	ERS	233	376	1.92
960620	980730	Descending	ERS	233	73	2.11
970220	970918	Descending	ERS	233	-213	0.58
970220	980312	Descending	ERS	233	-30	1.06
970220	980730	Descending	ERS	233	264	1.44
970501	970605	Descending	ERS	233	146	0.09
970501	970918	Descending	ERS	233	-122	0.38
970501	980101	Descending	ERS	233	485	0.67
970501	980312	Descending	ERS	233	62	0.86
970501	980730	Descending	ERS	233	356	1.25
970605	980101	Descending	ERS	233	339	0.57
970605	980312	Descending	ERS	233	-84	0.77
970605	980521	Descending	ERS	233	514	0.96
970605	980730	Descending	ERS	233	210	1.15
970918	971127	Descending	ERS	233	836	0.19
970918	980101	Descending	ERS	233	606	0.29
970918	980521	Descending	ERS	233	782	0.67
970918	980625	Descending	ERS	233	-556	0.77
970918	980730	Descending	ERS	233	478	0.87
971127	980101	Descending	ERS	233	-230	0.1
971127	980312	Descending	ERS	233	-653	0.29
971127	980416	Descending	ERS	233	-129	0.39
971127	980730	Descending	ERS	233	-358	0.67
980101	980312	Descending	ERS	233	-423	0.2
980101	980416	Descending	ERS	233	102	0.29
980101	980730	Descending	ERS	233	-128	0.58
980312	980416	Descending	ERS	233	524	0.09

980312	980521	Descending	ERS	233	599	0.19
980312	980625	Descending	ERS	233	-740	0.29
980312	980730	Descending	ERS	233	295	0.38
980416	980730	Descending	ERS	233	-226	0.29
980521	980730	Descending	ERS	233	-304	0.19
080906	090124	Descending	Envisat	462	-207	0.38
080906	090509	Descending	Envisat	462	-489	0.67
080906	090718	Descending	Envisat	462	-277	0.87
080906	090822	Descending	Envisat	462	-222	0.96
080906	100320	Descending	Envisat	462	-311	1.54
080906	100911	Descending	Envisat	462	-222	2.01
090124	090718	Descending	Envisat	462	-69	0.48
090124	090822	Descending	Envisat	462	-103.51	0.58
090124	100213	Descending	Envisat	462	317	1.05
090124	100911	Descending	Envisat	462	-15	1.63
090509	090718	Descending	Envisat	462	212	0.19
090509	090822	Descending	Envisat	462	177	0.29
090509	100213	Descending	Envisat	462	599	0.76
090509	100320	Descending	Envisat	462	267	0.86
090509	100807	Descending	Envisat	462	-170	1.24
090718	100213	Descending	Envisat	462	387	0.57
090718	100807	Descending	Envisat	462	-382	1.05
090822	100213	Descending	Envisat	462	420	0.48
090822	100320	Descending	Envisat	462	89	0.58
090822	100807	Descending	Envisat	462	-348	0.96
090822	100911	Descending	Envisat	462	89	1.05
100213	100911	Descending	Envisat	462	-332	0.58
100320	100807	Descending	Envisat	462	-437	0.38
100320	100911	Descending	Envisat	462	-0.19	0.48
100807	100911	Descending	Envisat	462	436	0.09
960113	980117	Descending	ERS	462	-337	2.01
971004	980117	Descending	ERS	462	-483	0.29
971004	980328	Descending	ERS	462	-267	0.48
971004	980502	Descending	ERS	462	65	0.58
971213	980117	Descending	ERS	462	409	0.09
971213	980328	Descending	ERS	462	625	0.29
971213	980711	Descending	ERS	462	96	0.58
971213	980919	Descending	ERS	462	125	0.77
980117	980502	Descending	ERS	462	548	0.29
980328	980711	Descending	ERS	462	-528	0.29
980328	980919	Descending	ERS	462	-500	0.48
980711	980919	Descending	ERS	462	-284	0.19

Appendix B

π-RATE produced InSAR rate map.

Since this study is to investigate the late postseismic deformation, π-RATE software is used to estimate a velocity rate map. Dr. Hua Wang re-processes all of four tracks original interferograms that listed in Appendix A. The Figure B5, B6, B7, B8 are interferograms after π-RATE software processing.

Figure B1, B2, B3, B4 are the removed topographically-correlated atmospheric delay error velocity maps along Tracks 276, 4, 233 and 462. Due to the limited acquisitions (Each track no more than 15 acquisitions), clear atmospheric patterns in the rate maps are shown. The red to blue transition zone shown on Track4 does not appear on Track 233 in the same area, which indicates the signal is coincidence. The same situation also appears in Track 233 and Track 462. On the Track 233, rate map in Figure B3., the red lobe locates at the north side of the fault, which shows a known left-lateral strike-slip movement. But on the final track T462, the overlap region between Track 233 and 462 have opposite signals. This discrepancy caused by atmospheric or topographic effect. More analysis on overlap areas in Appendix D also presents the variation on different tracks at the same location. In conclusion, the postseismic deformation signal cannot be robustly identified, which only permits lower bounds to be placed on the viscosity in this thesis.

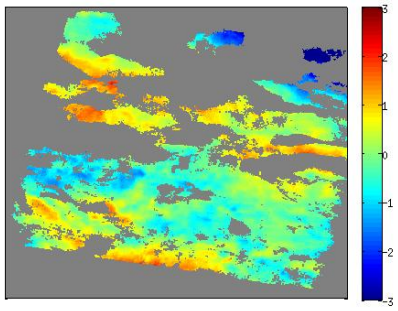

Figure B1. Track 276 rate map in mm/yr

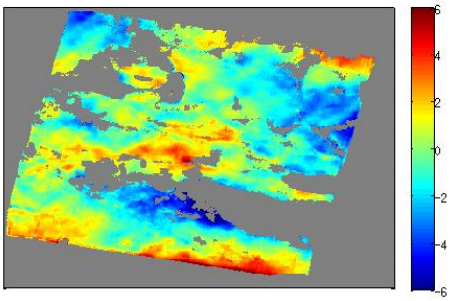

Figure B2.Track 4 rate map in mm/yr

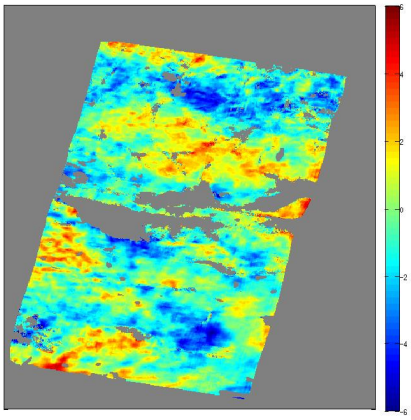

Figure B3.Track 233 rate map in mm/yr

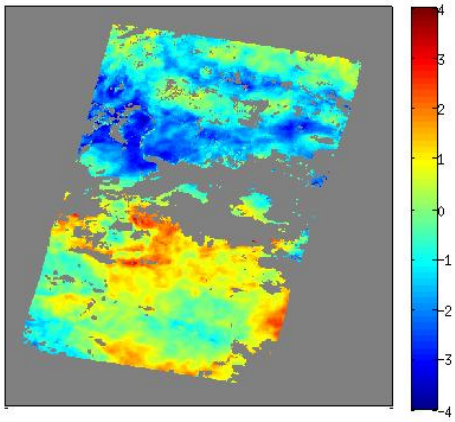

Figure B4.Track 462 rate map in mm/yr

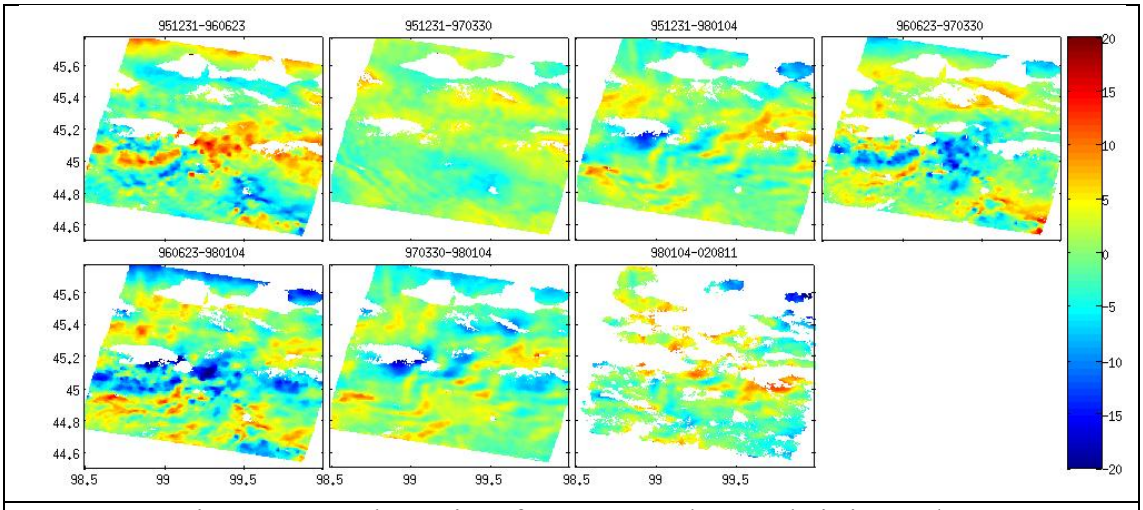

Figure B5.Track 276 interferograms, colour scale is in mm/yr

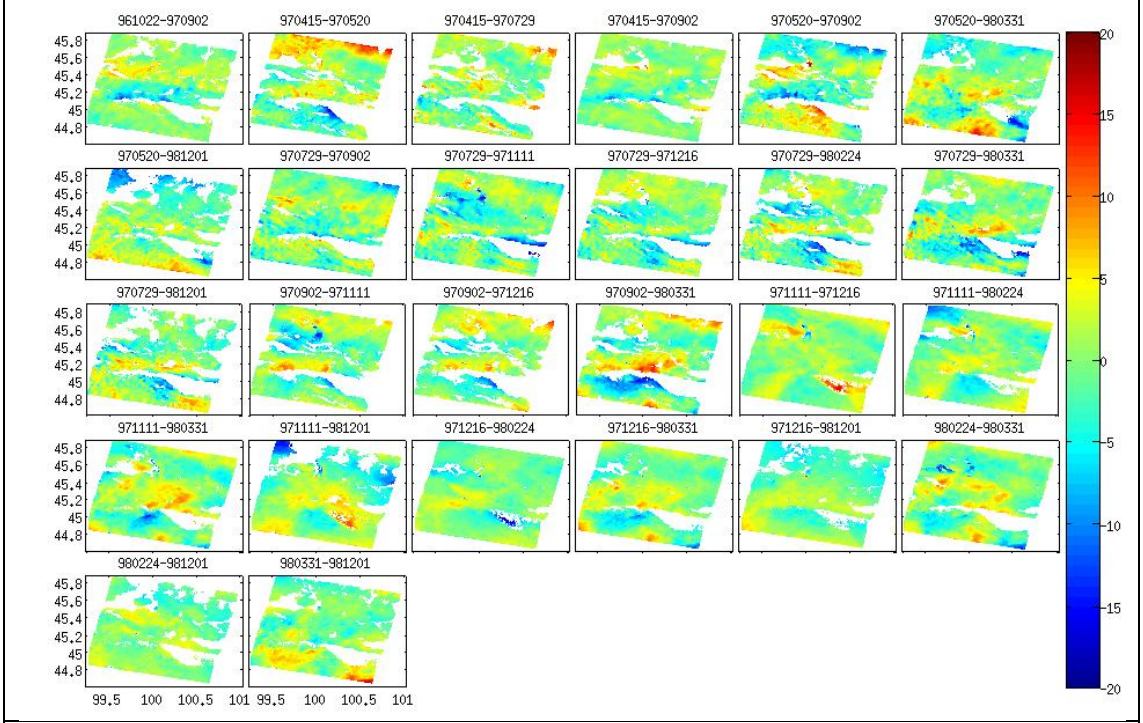

Figure B6.Track 4 interferograms, colour scale is in mm/yr

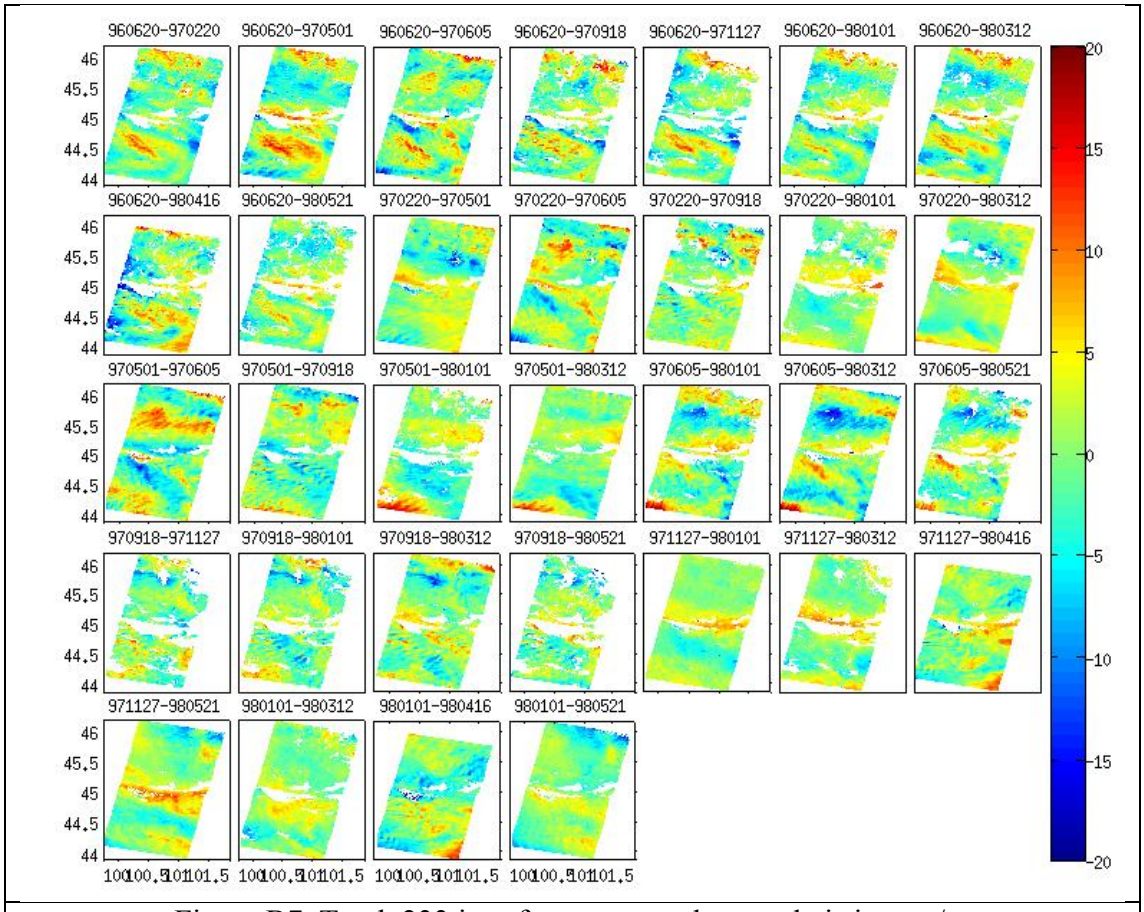

Figure B7. Track 233 interferograms, colour scale is in mm/yr

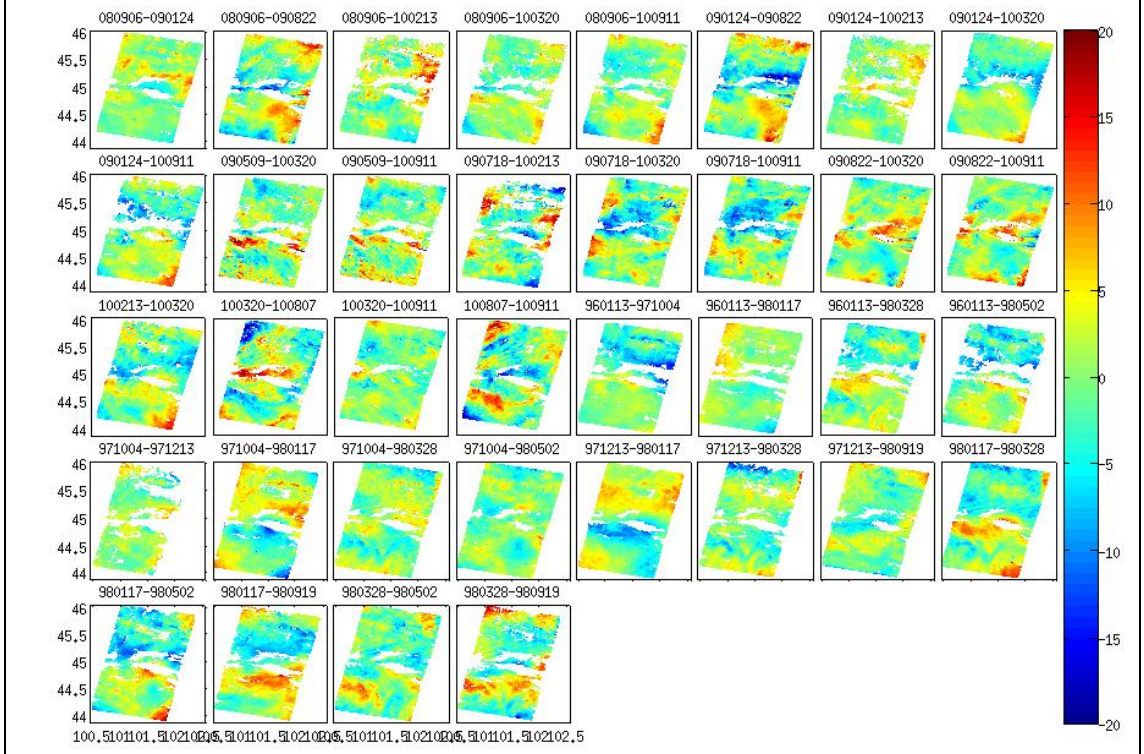

Figure B8. Track 462 interferograms, colour scale is in mm/yr

Appendix C

Viscoelastic relaxation models generate from VISCO1D.

Line of sight displacements predicted by models with two layers Maxwell body rheology. Lid over a viscoelastic half space case. Different models corresponding to increasing upper layer thickness (columns: 10 km, 15 km, 20 km, 30 km) and viscosity (rows: 1×10^{17} Pa s, 1×10^{18} Pa s, 1×10^{19} Pa s, 1×10^{20} Pa s, 1×10^{21} Pa s, 1×10^{22} Pa s, 1×10^{23} Pa s) were implemented. The elastic upper layer has shear modulus μ and the underlying layer has a viscous element with viscosity η. Colour scale is in -1~1 cm/yr.

Thickness Vs. Viscosity	10 km	15 km	20 km	30 km
1×10^{17}	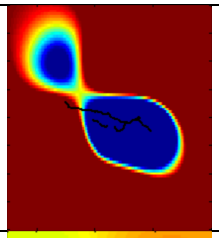	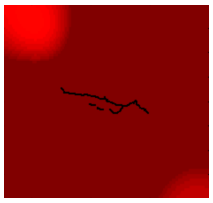	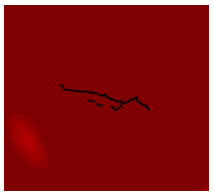	
1×10^{18}	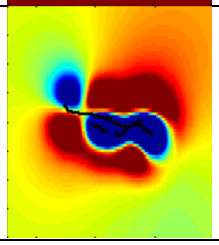	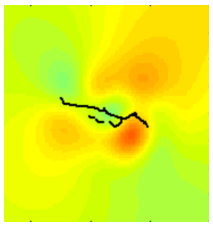	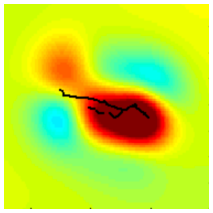	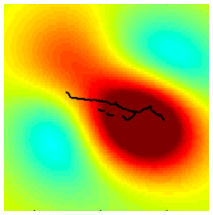
1×10^{19}	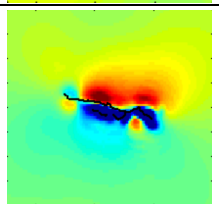	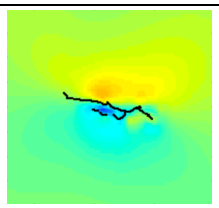	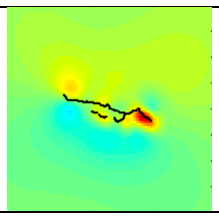	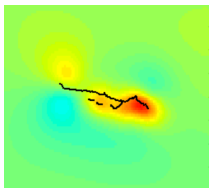
2×10^{19}	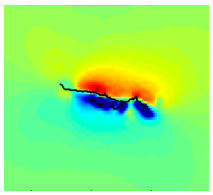	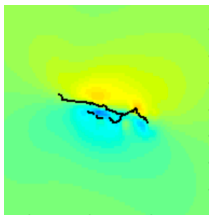	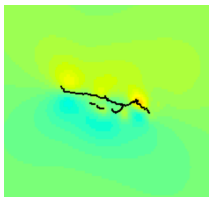	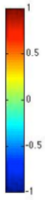
3×10^{19}	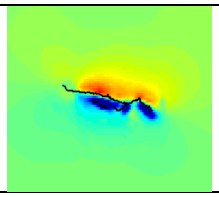			
4×10^{19}	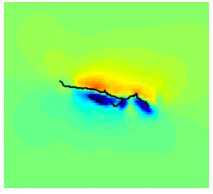	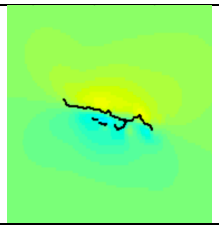	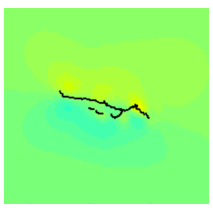	

5×10^{19}	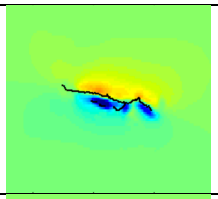			
6×10^{19}	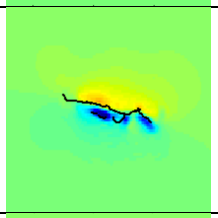	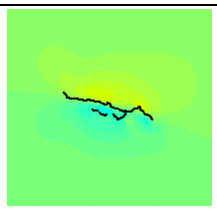	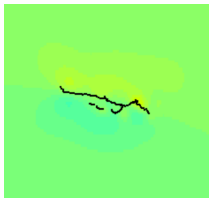	
7×10^{19}	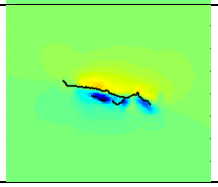			
8×10^{19}	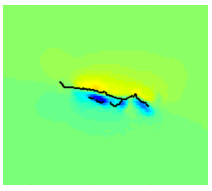	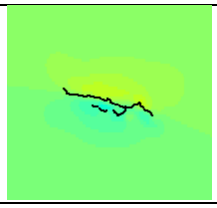	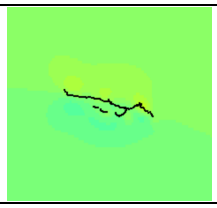	
9×10^{19}	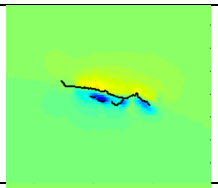			
1×10^{20}	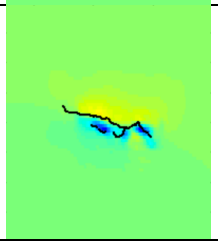	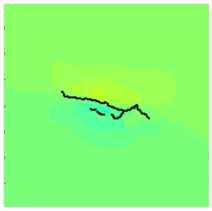	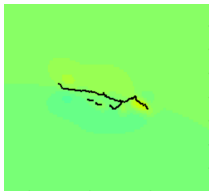	
2×10^{20}	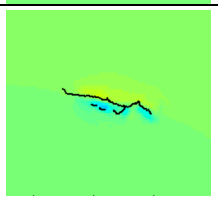	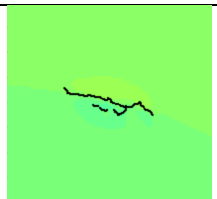	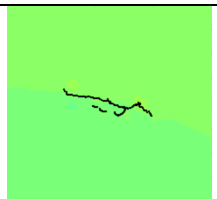	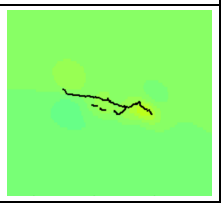
4×10^{20}	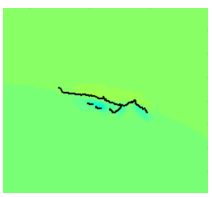	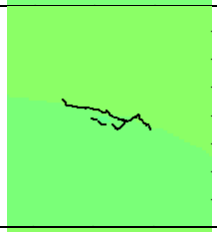	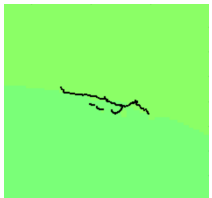	
6×10^{20}	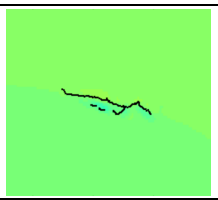	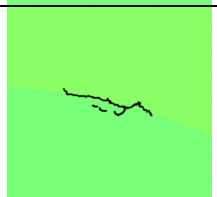	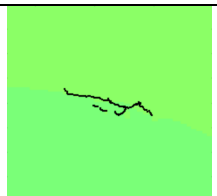	

8×10^{20}	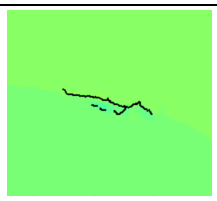	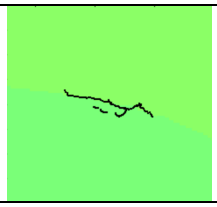	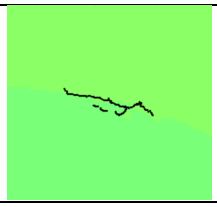	
1×10^{21}	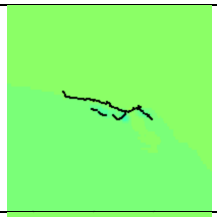	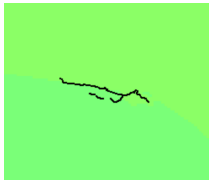	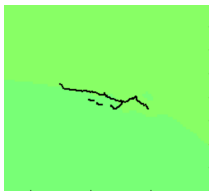	
2×10^{21}				
4×10^{21}				
6×10^{21}	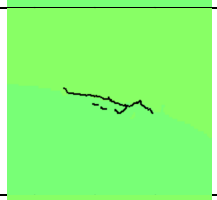			
8×10^{21}				
1×10^{22}	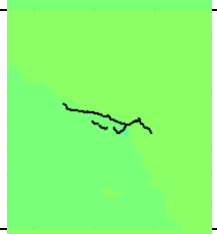			
1×10^{23}	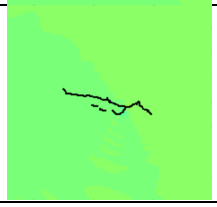	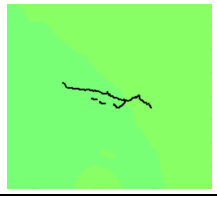	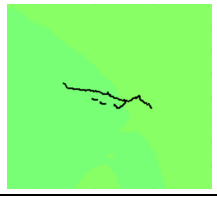	

Appendix D

InSAR rate map overlap area analysis on Tracks 276, 4, 233 and 462.

As can be seen that the scatter plot between different tracks shows varied values on the same i^{th} pixels, especially on Figure 1D and 3D. This phenomenon gives rise to the conclusion that the InSAR rate map including amount of noise. Further work need to improve the quality of InSAR observation.

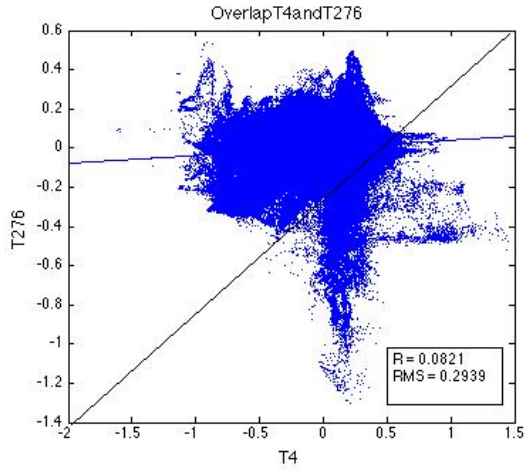	Figure 1D. X-axis is Track 4 InSAR overlap i^{th} pixel value, and y-axis corresponds to the same i^{th} pixel on Track 276 InSAR overlap area. Blue line is a least-squares line on the scatter plot.
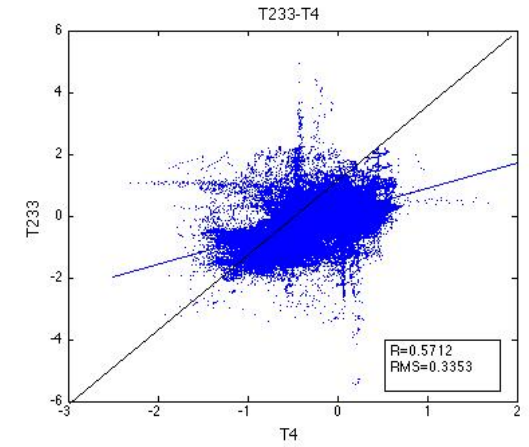	Figure 2D. X-axis is Track 233 InSAR overlap i^{th} pixel value, and y-axis corresponds to the same i^{th} pixel on Track 4 InSAR overlap area. Blue line is a least-squares line on the scatter plot.
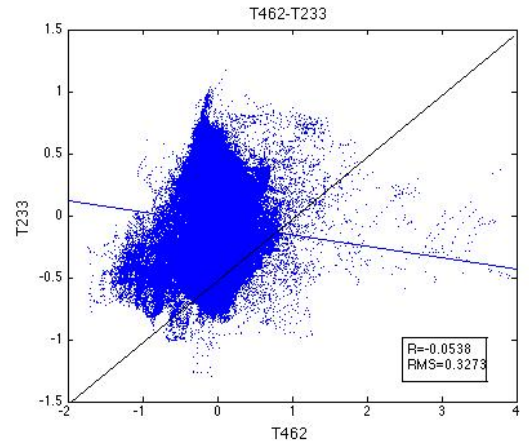	Figure 3D. X-axis is Track 233 InSAR overlap i^{th} pixel value, and y-axis corresponds to the same i^{th} pixel on Track 462 InSAR overlap area. Blue line is a least-squares line on the scatter plot.